Toward Functional Magnetic Applications for Multi-material Inkjet 3D Printing

by

Louise E. van den Heuvel

Submitted to the Department of Mechanical Engineering
in Partial Fulfillment of the Requirements for the Degree of

Master of Science in Mechanical Engineering

at the

Massachusetts Institute of Technology

June 2016

Signature of Author: Signature redacted
Department of Mechanical Engineering
May 20, 2016

Certified by: Signature redacted
Wojciech Matusik
Associate Professor of Electrical Engineering and Computer Science
Thesis Supervisor

Certified by: Signature redacted
A. John Hart
Associate Professor of Mechanical Engineering
Mechanical Engineering Faculty Reader

Accepted by: Signature redacted
Rohan Abeyaratne
Quentin Berg Professor of Mechanics
Chairman, Committee on Graduate Students

Toward Functional Magnetic Applications for Multi-material Inkjet 3D Printing

by

Louise E. van den Heuvel

Submitted to the Department of Mechanical Engineering

on May 20, 2016 in Partial Fulfillment of the

Requirements for the Degree of

Master of Science in Mechanical Engineering

ABSTRACT

The bounds of the design space for 3D-printed objects continue to rapidly extend as the library of printable materials continues to grow. This thesis explores printed objects uniquely enabled by the addition of a magnetic ink to the existing repertoire of materials for the MultiFab printer, a high-resolution, multi-material inkjet 3D printer. Magnetic nanoparticles, a base ink, and a dispersion method are selected to develop the magnetic ink. The ink is optimized for maximal magnetic content and its magnetic properties are characterized. A 9.7 ± 0.8 wt% magnetite ink with expected stability exceeding 10 days is achieved. Design, characterization, and validation of two small-scale multi-material actuators driven by magnetism is performed. The first actuator is a simple fixed cantilever, while the second is a tilting panel. More advanced structures and actuators are explored and are suggestive of an extremely wide scope for potential future applications. The fields of application shown for 3D-printable magnetic ink in a multi-material context range from biomimicry (e.g. stimuli-responsive surfaces) to optics and aerodynamics.

Thesis Supervisor: Wojciech Matusik

Title: Associate Professor of Electrical Engineering and Computer Science

ACKNOWLEDGEMENTS

Thank you to my advisor, Professor Wojciech Matusik, for his guidance throughout my research. I also thank Professor John Hart for being the Mechanical Engineering faculty reader for this work.

I would like to thank the Computation Fabrication Group for providing the context for this work and endless feedback and assistance along the way. I am especially thankful to Subra and Melina for their extensive collaboration of thoughts and to David for assisting with ink preparation and material characterization.

Lastly, I must also thank my friends and family, and especially Jeff, for their enduring support.

Contents

List of Figures

List of Tables

1 Introduction

As the library of 3D-printable materials continues to expand, so does the related design space of functional applications. Magnetic materials are especially exciting due to their ability to enable safe, untethered, remote, and massively parallel actuation of structures. This work explores the development of a magnetic ink that is designed to be added to the existing material repertoire of the Computational Fabrication Group's micron-resolution, multi-material inkjet 3D printer. The multi-material context provided for magnetic ink is important, because it broadens the scope of applications enabled by the technology. Notably, magnetic materials on their own commonly do not generate enough force to cause significant deformation of the bulk material. The coupling of compliant materials or geometries with magnetic structures can allows a greater range of deformations for a given force. For example, this becomes salient when trying to mimic responsive surfaces with small-scale actuators in nature, such as goosebumps on skin or structural coloration mechanisms in animals that use camouflage. The scope of this work is further enhanced by a complementary multi-material topology optimization program simultaneously developed in the lab. By programmatically combining rigid, flexible, and magnetic materials in a single print, we can fabricate finely controlled, magnetically responsive actuators with the potential to enhance biomimetic, optical, aerodynamic, and other functional applications.

The design of practical applications for inkjet 3D printing includes material development, theoretical modeling, and experimental measurement and validation. Material development entails particle and dispersion method selection, as well as experimentation regarding the upper limits of particle concentration (see Section 1.5). A final formulation is determined and characterized (see Section 2.5). Cantilever and simple tilting panels are designed to characterize the deformations achievable through magnetic actuation (see Section 4.1 and Section 4.2). Additionally, more complex structures are designed to suggest more complex applications (see Section 4.3). The actuators are simulated with magneto-mechanical modeling (see Section 5). The magnetic field and deflections of the cantilevers is measured and compared to the theoretical model (see Section 6.1 and Section 6.2). Measurement of tilting panel deflections are made and used to drive a tilting panel

simulator and optimizer (see Section 6.3). Lastly, further recommendations for magnetic 3D printing in the context of MultiFab are made (see Section 7.2).

1.1 Motivation for Work

3D printers are well known for their ability to enable rapid prototyping of bespoke parts. As additive manufacturing exploded onto the marketplace, 3D printers often faced criticism for only being able to produce parts that mimic the form of real parts, and not the functionality. However, much recent work in industry and especially academia indicates that additive manufacturing not only has the ability to create functional parts for a vast variety of applications, but even has the ability to create parts with functionality beyond standard manufacturing techniques.

There has been work in additive manufacturing ranging from mimicking tissues[1] to fabricating electronics[2]. A number of researchers have been able to take additive manufacturing a step further by adding additional "dimensions" beyond the traditional three-dimensional shaping capabilities. Further "dimensions" can be considered in prints that have additional parameters to control besides the shape. Common themes for a fourth dimension are usually a combination of programmable anisotropy and predictable shape-morphing functionality[3–7]. Products created with this fourth dimensions are often referred to as smart materials[8]. For example, Mark Guttag and Mary Boyce at MIT created locally and dynamically controllable surface topography (+1D) by imbedding hard particles in soft print structures[3]. Kokkinis et al. magnetically align stiff platelets in their prints, which enables local control of composition (+1D) as well as particle orientation (+1D) such that they can claim five-dimensional control[9]. These programmable objects are not easily fabricated by previously existing manufacturing methods.

Notably, programmable anisotropy brings us closer than ever before to replicating important mechanisms in nature[4,10–13]. For example, A. S. Gladman et al. recently created 3D-printed bi-layers with anisotropic swelling (+1D), like that of cell walls, which was programmatically assigned to achieve target shapes when immersed in water. However, there are still limitations in terms of what can be replicated. There is a lack of technology that allows us to imitate non-uniform arrays of soft, micron-scale, moveable surface

structures[14], such as goosebumps on skin[15], coloration mechanisms used for animal camouflage[16], or the moveable scales seen on sharks[17,18].

Toward replicating these functional structures, the ability to print magnetic material in a multi-material context is particularly enticing. Magnetism is a unique source of force in its ability to create instantaneous and dynamic actuation over a continuous tuning range[19]. Beyond this, it also has the ability to enable massively parallel untethered actuation and is generally safe. However, magnetic material has its limitations. Magnetic materials on their own commonly do not generate enough force to cause significant deformation of the bulk material[20]. This is why the pairing of compliant materials or geometries with magnetic structures is important. It can allow a greater range of deformations for a given force, making actuation of small-scale structures more achievable. Moreover, the MultiFab platform (see Section 1.2) includes a topology optimization framework that, driven by design specifications, enables the highly desirable capability to program smart materials. By adding magnetism to this computer-aided smart material design framework, we have a tool that allows us to create finely-controlled, micron-resolution soft actuators.

However, the design space enabled by the proposed technology goes can go well beyond biomimetic soft actuator arrays. The ability to smartly, i.e. programmatically, incorporate magnetic material into a multi-material print can significantly widen the scope of the additive manufacturing design space as a whole, and that is perhaps the true motivation of this work. By adding magnetic ink to an already versatile material repertoire, new functional applications for this 3D printing technology can be inspired by virtually anything that involves magnetism, although the specialty of inkjet printing would be smaller-scale technologies that require micron-scale resolution. There is a myriad of interesting applications for magnetically responsive structures[21–27]. It is the hope of the author that this work serves as a stepping stone for more streamlined fabrication of many of those applications, from small autonomous robots[27] and electromagnetics[28] to assembly methods for nanostructures[29], or for more biologically inspired magnetic actuators such as artificial flagella and cilia[30,31]. Besides actuation, the magnetic material could also be used for sensing, such as the magnetoreceptors found in honey bees[32], or magnetic heating[33] applications.

1.2 MultiFab

MultiFab[34] is a low-cost, high-resolution inkjet 3D printing platform that was designed by the Computational Fabrication Group (CFG) to be modular and extensible. It can support the printing of up to ten different materials at once and achieves resolution of at least 40 μm. CFG specially develops inks for the print such that they are jettable, or able to be reliably ejected by the printhead, and also to have desired characteristics such as high strength or flexibility (see Section 1.3). The platform is extensible in that it enables seamless addition of print enhancing modules such as additional heaters to evaporate precipitates or even a machine vision module that allows for closed loop feedback to enable print corrections. Figure 1.1, shows the MultiFab printer used for this work. Section 1.2.1 describes the printer in further detail.

Figure 1.1: The MultiFab printer used for this work is shown in the photo, courtesy of Javier Ramos.

As the MultiFab printer and its material library continue to be developed, a number of practical applications have already been demonstrated. The printer can only be as impressive as the materials that it prints. The existing material library for the printer includes materials with a wide range of optical, mechanical, and appearance properties. So far, published applications for the printer have only included samples with optical and mechanical interactions, though work on other unique materials is ongoing at the time of writing. Figure 1.2 shows a few sample applications already achieved by the printer: functionally graded materials, fiber bundles, and caustic devices. Section 1.2.2 describes the materials that are critical to this work.

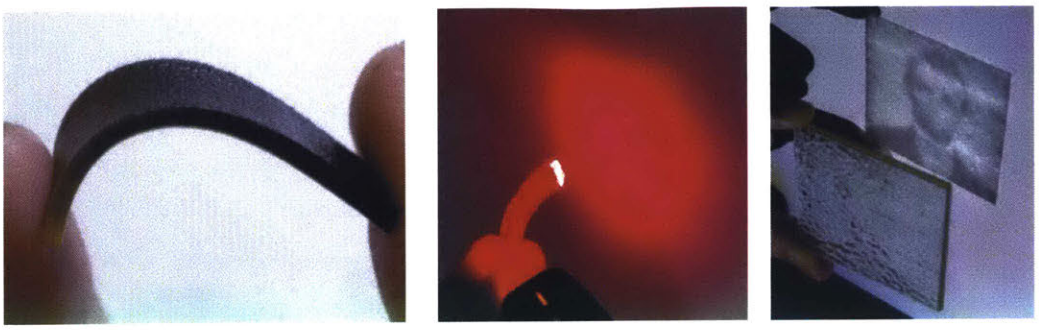

Figure 1.2: Photographs display sample applications already achievable by MultiFab: functionally graded materials (left), fiber bundles (center), and caustic devices (right). Images courtesy of Javier Ramos.

1.2.1 MultiFab Platform

The printer used in this work is a smaller version of the printer described by P. Sitthi-Amorn et al.[34] Figure 1.3 shows a simplified schematic highlighting the critical modules of the printer used for this work: a heated printhead, pressurized ink bottles, a positioning system, and a UV unit. The single printhead has five channels, which enables printing of up to 5 materials in a single layer, which is all that is needed for this work. The bottles contained the print materials in uncured, or liquid, form; they are pressurized by a pressure control system (not shown) to ensure that the necessary fluid pressure at the inlet of the printhead is maintained. A XY-gantry is used to move the printhead in a plane above the print platform. Because the height of the XY gantry is fixed, the printing platform sits on lead screw drives for control in the Z-direction. The UV unit is used to solidify the ink.

To actually print a part, a user must import a voxelized 3D model and bring it into the

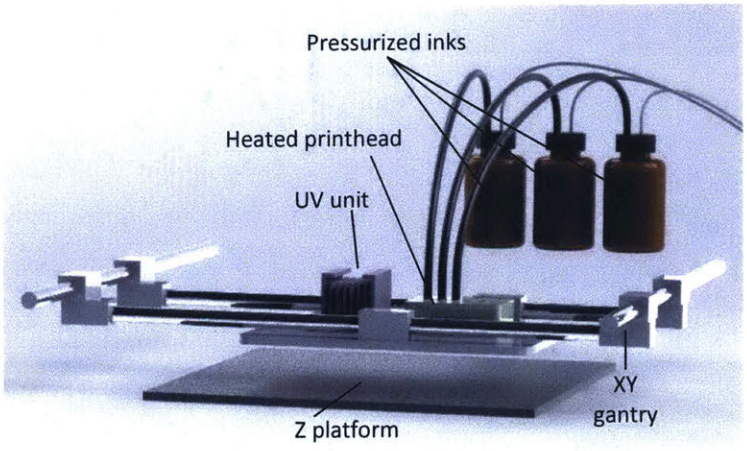

Figure 1.3: Simplified schematic of the version of the MultiFab printer used for this work, featuring the pressurized ink bottles, heated printhead, UV unit, and motion system.

proprietary print software known as Fabricator, with each voxel assigned to a material ID. The data for the part is sent to the printer in a layer by layer fashion, from bottom to top. The printhead is moved and the appropriate materials are jetted out by the printhead to the correct positions. The layer is solidified by passing over it with the UV unit, and then the process is repeated until the part is complete.

1.2.2 CFG Material Library

Naturally this work focuses on the newly developed magnetic material, or ink, as described in Section 1.5. However, this work also relies heavily on two materials previously formulated by CFG, a rigid material, RIG, and a flexible material, ELA. These two materials were designed to span several orders of magnitude in terms of stiffness. Both materials are UV curable photopolymers that are translucent. However, RIG has a Young's Modulus on the order of hundreds of megapascals, closer to traditional plastics, while ELA has a Young's Modulus on the order of hundreds of kilopascals, closer to weak rubbers. The specific formulations used for this work are RIG 8.1 and ELA 7.2, but they are referred to as RIG and ELA, respectively, equivalently throughout this work. Please see Appendix A for the full names of all components in each ink as well as suppliers and ratios for ink formulation.

In order to enable fully freeform, three-dimensional prints, support material must also be used. In general, parts were strategically designed to avoid the need for support material, because CFG's support material is still in development at the time of writing. However, Section 4.3.3 does introduce the use of an epoxy-based formulation, EPX-100, as a wash-away support. The EPX-100 is formulated without photo-initiator so that it does not solidify during the print process.

"Magnetic ink" used throughout this work refers to any base ink with dispersed magnetic nanoparticles. "Magnetite ink" refers to an ink that specifically contains iron oxide (Fe_3O_4) particles. Because this is the ink that receives the most attention in this work, it is referred to as FEO as a shorthand equivalent to RIG and ELA. Specific formulation details are noted when relevant.

1.3 Inkjet Inks

Inkjet 3D printers are limited to materials that are, in short, jettable and curable. What this means for inkjet printers in general is that the material must pass through the printhead in a liquid state and have the right rheological properties to be ejected from the printhead, and then be able to solidify through a process compatible with the printer in question. Inks must fall within a certain range for density, ρ, surface tension, γ, and shear viscosity, η, considered simulataneously[35]. There are several dimensionless parameters based on these properties that are useful for determining whether or not an ink is printable: Reynolds (*Re*), Weber (*We*), and Ohnesorge (*Oh*) numbers. Their equations are as follows:

$$Re = \frac{v\rho a\gamma}{\eta}, \tag{1}$$

$$We = \frac{v^2\rho a}{\gamma}, \tag{2}$$

$$Oh = \frac{\sqrt{We}}{Re}, \tag{3}$$

where v and a are the velocity and characteristic lengths, respectively, of the print droplet, which is largely dependent on the nozzle size of the printer. Derby 2010 shows that if the Reynolds numbers and the Weber number are plotted in a 2D coordinate system, a set of inequalities can be used to define a region in which the fluid is printable. Two governing inequalities are based on the inverse of the Ohnesorge number, the Z number,

$$Z = \frac{1}{Oh}. \tag{4}$$

First, if $Z < 1$, the fluid is too viscous for printing. Second, if $Z > 10$, the fluid is not viscous enough which will cause the undesirable formation of excess droplets, known as satellite droplets.

Beyond the aforementioned parameters, there are a few other factors that can disqualify an ink from being printable. For example, the fluid must be curable. This work relies on photopolymer inks that contain photo initiators such that exposure to a UV light solidifies them. Furthermore, the ink must be chemically compatible with the printing system such that the feeding system is not compromised during printing. MultiFab uses the commercial printhead of an Epson Workforce 30 2D printer. This piezoelectric drop-on-demand

printhead features 600 DPI resolution, and nozzles that can eject droplets ranging from 6 pL to 26 pL in volume. Each of its 540 nozzles has a diameter of 30 microns. This nozzle size is important not only in terms of how it affects the aforementioned dimensionless parameters, but also because it imposes one final constraint on the print material: the fluid must pass through without clogging the printhead. CFG indicates that inks with particles greater than 1 micron in diameter will cause clogging of the nozzles and are therefore not jettable. For this reason, all inks are passed through a 1-micron filter before loading them onto the printer.

More often than not, CFG has experienced that a change shear viscosity is what drives a fluid out of the printable region, because the other parameters are relatively stable. Based on the inks used in CFG, the upper bound of the printable viscosity range is approximately 16 cP. Adding nanoparticles generally increases the viscosity of a fluid such that the base formulation must be adjusted to keep the fluid in the jettable range at printing conditions. Section 2.3 further discusses methods used to develop the ink within the printable range.

After an ink is measured within the printable viscosity range, the final step toward reliable use of the ink in a print is developing a waveform for the ink. The waveform is a set of voltage instructions sent to the printhead. The changing voltage actuates the piezoelectric material in the nozzle chamber, ejecting a droplet. This action must happen reliably in order to fabricate a high quality print.

1.4 Magnetic Nanoparticles

Magnetism is an intriguing source of force for actuation. It is generally safe and biologically friendly, and offers the highest manipulation forces and torques for soft matter when compared to acoustic, optical, or electric fields[20]. It can be used to simultaneously actuate many parallel structures, remotely and wirelessly. Section 1.4.1 explains important magnetic properties referred to in this work. Of course, achievable forces are entirely dependent on the specific magnetic materials in use. The fabrication method for this work forces magnetic nanoparticles to be the primary material of interest. There has been previous work with magnetic nanoparticles in inkjet printing, but some problems remain (see Section 1.4.2).

1.4.1 Fundamental Magnetic Properties

Magnets are divided into two groups, soft and hard[36]. Hard magnets are the materials that are referred to colloquially as "permanent" magnets, while soft magnets are the materials that are colloquially simply described as "magnetic" or able to be attracted by a magnet. Soft magnets are essentially temporary magnets; they are only significantly magnetic when in the presence of a magnetic. Three fundamental parameters that can help describe a magnetic material are saturation mass magnetization (M_S), remanence (M_R), and coercivity (H_C). All three properties can be drawn from the measurement of a magnetic hysteresis loop, or B-H curve, which follows the magnetization of a material (B) based on magnetic field strength (H). The SI unit for magnetization or magnetic flux density is the Tesla. Magnetic field strength is measured in Amperes per meter. However, Gaussian units are still commonly used in the field of magnetics, and thus will be used to report some values in this work to allow easy comparison with supplier data.

During measurement of a magnetic hysteresis loop, the magnetic material is exposed to a high magnetic field, which is subsequently removed. The saturation magnetization, B_S, is the maximum measured magnetic flux density, divided by mass to indicate mass magnetization. Saturated mass magnetization is M_S, reported in the Gaussian units of emu/g, as is a common convention in magnetic work. All magnetic materials gain magnetization when exposed to a magnetic field, but when the field is lessened, some materials lose magnetization sooner than others. Remanence is the residual magnetism after the field has been returned to zero. Hard magnets have high remanence (~.5+ T), while the remanence of soft magnets is negligible. Remanence is also divided by mass and reporter in emu/g. Lastly, coercivity describes how soon a magnet loses its magnetization when exposed to a field, and corresponds with the measurement of the magnetic field when the magnetization of a material falls to zero. This is reported in the Gaussian units of Oersteds (Oe). As a result of the aforementioned details, a soft magnet has a very narrow hysteresis loop compared to a hard magnet[36].

1.4.2 Use in Printing

The materials explored in this work are all nanopowders. This is partly due to the limitation imposed by the nozzle diameter, 30 microns. However, a more important feature

particular to magnetic particles at this scale is that, even when magnetic, they are not inherently attracted to one another[37]. If they were, it could be impossible to print with them despite their small size relative to the nozzle diameter, because they would agglomerate. Agglomerations are troublesome for a number of reasons[38]. Large enough agglomerations will clog the printhead. Smaller agglomerations may be jettable, but could still cause material imperfections leading to a more brittle part. Magnetite in particular is denser than most fluids used for inkjet printing. Due to their relatively large surface area, single particles are able to remain suspended in the fluid. Agglomerations, overcome by gravitational forces, will settle to the bottle of the liquid over time[39]. Ideally, the magnetic ink should be a colloid, a solution with evenly distributed particles.

The most utilized nanoparticle for this work was magnetite, a form of iron oxide with the chemical formula Fe_3O_4. Because of its spherical nature, it has limited capacity for enabling the magnetic anisotropy necessary for hard magnetic applications. Magnetite is a popular nanoparticle in research, and its use in a variety of applications, such as magnetic storage, biosensing, and targeted drug delivery, is well-documented[40]. It is particularly common in biomedical applications because it readily accepts surface coatings that make the particles non-toxic and biocompatible[41]. Previous research regarding the use of iron oxide particles in inkjet printing was generally limited to 2-dimensional applications[42]. Clay 2015 demonstrates a 3D-printable magnetic ink, but the dispersion lacks stability to maintain a constant loading, even between two subsequent layers of a single print[43], which makes it insufficient for creating predictable structures. This work seeks to improve upon the ink stability, in addition to exploiting the wide scope enabled by the multi-material context.

1.5 Thesis Contributions

Magnetic nanoparticle dispersion and clogging issues are overcome to achieve a formulation of a 3D-printable magnetite ink with a nanoparticle concentration of 9.7 ± 0.8 wt%. The ink has an expected stability in excess of 10 days, improving upon the stability seen in prior art[43]. For the first time, micron-resolution multi-material magnetic actuators are fabricated in a single 3D print, and they require no post-processing. Measurements of these actuators serve as the foundation for the vast range of applications enabled by adding magnetic material to the existing multi-material inkjet 3D printing repertoire.

2 Ink Development Methods

Toward the overarching goal of enabling novel magnetically-related applications for 3D printing, the first step was creating a reliably jettable (see Section 1.3) ink containing magnetic nanoparticles. There had been some previous exploration of nanoparticle incorporation into CFG materials. These results were initially used to guide the selection of nanopowders that could be viable for printing as well as potential base fluids to carry the nanoparticles. The most successful was a 5 wt% suspension of hydroxyapatite nanoparticles (<200 nm particle size, Sigma-Aldrich, USA) in RIG. Results indicated that this increased the stiffness, strength, and toughness of the control material (RIG), which was desired[38]. An ultrasonic mixer was used to disperse the particles, and the inks remained stable (no significant settling was observed) for several weeks, thus the majority of tests suspensions of magnetic nanoparticles in RIG, dispersed using the ultrasonic mixer.

Methods for ink development are described in the following sections. After particles were ordered, different techniques were explored for dispersing the nanoparticles in a printable fluid. After narrowing down potential nanoparticles, a base fluid, and dispersion method, one of the last steps was attempting to increase the percent weight loading of the nanoparticles in the base fluid. Regardless of the nanoparticle type, it was desirable to maximize the percent weight content loading of the nanoparticles in the ink. The higher the loading of a given particle, the greater the magnetic forces that are enabled for a given geometry.

2.1 Particle Exploration

Nanoparticle selection was driven by potential ability to satisfy printing conditions, magnetization, and to some degree, cost constraints. Previous literature indicates better dispersion results when particles were synthesized and coated with dextran to prevent agglomeration[44]. Due to limited capacity in CFG to synthesize the particles, ready-made nanoparticles were ordered from material providers such as Sigma-Aldrich, USA, and US Research Nanomaterials (US Nano), Inc, USA. Particles that were less than 200 nanometers, had known magnetic properties, and were under $100 for 25 grams, were ordered. Table 1

summarizes the particles that were ordered. Section 3.1 describes preliminary results that helped narrow down the particle choice.

Table 1: List of powders ordered as potential constituent of magnetic ink. M_S is saturation mass magnetization, H_C is coercivity, and M_R is mass remanence.

Powder	Supplier	Size (nm)	Reported magnetic properties
PVP-coated iron oxide (Fe_3O_4)	US Nano	15-30	M_S=60.45 emu/g, H_C=30.98 Oe
Cobalt iron oxide ($CoFe_2O_4$)	US Nano	30	M_S=46.8 emu/g, M_R=17.3 emu/g, H_C=900 Oe
Nickel iron oxide ($NiFe_2O_4$)	US Nano	30	M_S=37.7 emu/g, M_R=5.3 emu/g, H_C=65 Oe
Iron oxide (Fe_2O_3)	Sigma-Aldrich	<50	Not reported.
Cobalt oxide (Co_3O_4)	Sigma-Aldrich	<50	Not reported.

To allow for comparison, the same dispersion method of ultrasonification (see Section 2.2.1) was initially used for all particles. This method was selected due to existing equipment constraints and time constraints. After dispersion, the mixture is assessed qualitatively to see if settling, or separation, had occurred. Figure 2.1 shows an example of an ink with poor dispersion quality; there is significant sedimentation within two days of dispersion. If the ink passes this qualitative inspection, it was then passed through the same 1-micron filter that is used to filter all inks in preparation for printer. Clogging or significant separation of the nanoparticles and the base ink during filtration would generally disqualify an ink. The last tests were viscosity measurement and drop analysis (see Section 2.3 and 2.4, respectively).

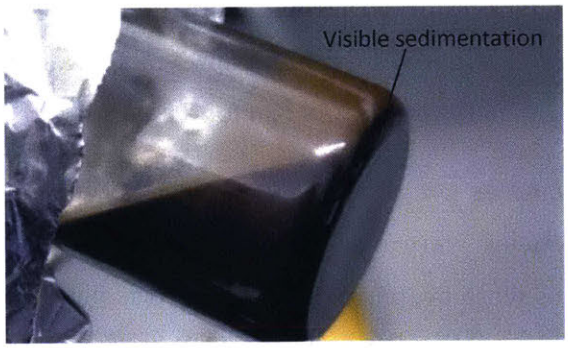

Figure 2.1: Photo showing poor dispersion; there is significant settling at the base of the bottle within two days of dispersion with the ultrasonicator.

2.2 Dispersion Methods

Four different methods of dispersion were explored: ultrasonicator, industrial immersion blender, bead mill, and pre-dispersion. Note that if the particle concentration is referred to as "[value] added wt%," it means that the weight percent is calculated from the weight of the original solution, rather than the total solution with the added particles. For example, with a base fluid of 100 g, 10 added wt% means that 10 g of nanoparticle was added to 100 g of base ink, making the actual wt% closer to 9 wt%. Results of the methods are discussed in Section 3.2.

2.2.1 Ultrasonicator

The same ultrasonic processing method used for the hydroxyapatite dispersion was used for this work. RIG was loaded with 1 added wt% nanoparticles. The mixture was inserted into the ultrasonicator (Industrial Sonomechanics, USA) and processed for one hour on pulse mode (10 s on, 10 s off). Because the process heats up the mixture, the container was partially immersed in ice water, which was replenished through the process. The length of processing was chosen, because increasing the processing time beyond this did not improve results.

2.2.2 Industrial Immersion Blender

A handheld, industrial quality immersion blender was used to process RIG with 1 added wt% nanoparticles. The mixture was processed for 30 minutes at "turbo" speed.

2.2.3 Bead Mill

An M100 Mini Mill (EMI, USA) was acquired based on literature indicating potential for high quality nanoparticle dispersion with this mixing method[45,46]. Once again, RIG with 1 added wt% nanoparticles was used for preliminary tests. The mill was loaded with the mixture and 500-micron diameter beads and run for 7 hours.

2.2.4 Pre-Dispersed Mixtures

Some magnetic nanoparticles were available from material suppliers pre-dispersed in water. If the nanoparticles were properly dispersed, it was possible that the mixture could be used in 3D printing by jetting the colloid and then evaporating the water with an

additional heating module. Fe_3O_4 20 wt% in water (US Nano) and Fe_2O_3 10 wt% (Sigma-Aldrich) in water were tested.

2.3 Base Ink Selection and Increasing Loading

It was necessary to ensure that the ink's viscosity stayed within the jettable range when at the standard heated printhead operating temperature, 70 °C. Adding nanoparticles to the base ink changes its rheological parameters. Though there are equations that can help predict viscosity of a fluid based on the concentration of spherical particles[47,48], CFG relies on measurement-driven fluid optimization. Aside from the water dispersions described above, RIG, ELA, and EPX (see Section 1.2.2) were considered as a base to which the nanoparticles were added. These inks are well understood by CFG and have a reliable jetting history.

A Brookfield viscometer was used to measure the viscosity of the magnetic inks. The viscometer includes a heating system such that the temperature of the ink can be adjusted while the viscosity is measured. The ink viscosity was noted at temperatures between 25 °C and 70 °C. These bounds were chosen to gain an understanding of what viscosity was like near room temperature as well as how it changes as it approaches printing temperatures. It would be possible to bring the printhead temperature to a value other than the standard operating temperature of 70 °C; however, it was preferable to avoid this in order to enable stable simultaneous printing of RIG and ELA. Sometimes, the RPM was adjusted to ensure that the viscosity measurement fell in a readable range. The slowest RPM that enabled a reading was always chosen.

When an ink's viscosity was found to be out of the printing range, the ink formulation was adjusted. For example, to decrease the viscosity of RIG a higher proportion of Gen1117, a low viscosity monomer, can be quickly incorporated into the dispersion through vigorous shaking. BYK110, mainly used to aid with stability of the dispersion, can also lower the viscosity of the mixture.

Each magnetic ink formulation is started with any measured amount of the base material. Then, addition of nanoparticles, BYK110, and Gen1117 are made as added weight percent to the original amount of base material. After the nanoparticles are dispersed, the ink is

weighed and a standard amount of photoinitiators are incorporated as an added weight percentage based on the new amount of ink (3 added wt%). Therefore, the ink is uniquely identified minimally by its base ink, nanoparticle, and added weight percent of the magnetic nanoparticles (MNP), BYK110, and Gen1117. As such, they are named with the following convention: [base ink]-[added wt% of MNP]%[MNP name]-[added wt% of BYK110]%BYK-[added wt% of Gen1117]%GEN. As an example, the most frequently formulated ink starts with a 200 g base of RIG. 30 g, 10 g, and 20 g, of magnetite (Fe_3O_4), BYK110, and Gen1117 are added, respectively. This ink is referred to as RIG-15%FE3O4-5%BYK-10%GEN. It should be noted that the maximum expected wt% of nanoparticles in the final print is always less than the listed added wt%. For example, in the aforementioned ink, if no nanoparticles or ink is lost throughout the process, the expected actual weight percent, as opposed to added weight percent, would be 11.2 wt%. Additionally, during the formulation process, some ink and nanoparticles are lost; this makes it important to measure the nanoparticle content after the formulation process is complete, ideally using a sample from an actual print.

2.4 Drop Analysis

When an ink is deemed to have the appropriate rheological properties for printing, a simulated printing set-up was used to analyze the droplets. JetXpert (ImageXpert Inc., USA), a high-speed camera, is used to observe droplets as they are ejected from the printhead, which is heated to 70 °C as it would be in the actual printer. JetXpert was used measure the average drop velocity and volume. The waveform is optimized until the droplets jetted out with no satellite droplets. Additionally, the drop volume and velocity was optimized to be similar to that of RIG: 22 pL to 28 pL for volume and 3 m/s to 4 m/s for velocity. This helps to prevent errors due to sizing and placement mismatches with other materials during printing. Figure 2.2 is a photograph showing magnetic ink droplets via JetXpert. The ink droplets show satisfactory jetting; they are relatively aligned, evenly spaced, and there are no stray droplets. Once an ink jetted out consistently for at least ten minutes within the JetXpert set-up, it was considered suitable for use in the MultiFab printer.

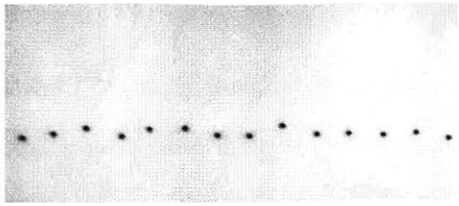

Figure 2.2: Image of magnetic ink print droplets as seen via JetXpert. The droplets show satisfactory jetting.

2.5 Test Prints and Characterization

The first prints made using a new magnetic ink were simple single-material solids, such as rectangular prisms. These structures were printed to ensure that the ink could be properly cured and used for larger 3D structures. Additionally, the first prints allowed qualitative assessment of the scale of force or actuations that might be generated with the materials. Secondary prints were samples used for material characterization. Measurements included Scanning Electron Microscope (SEM) imaging, Thermogravimetric Analysis (TGA), Vibrating Sample Magnetometer (VSM) measurement, and tensile testing.

2.5.1 Scanning Electron Microscope (SEM)

An arbitrarily sized bulk sample was printed and cut for imaging using a Zeiss Merlin high-resolution SEM. The sample was coated with 5 nm Au (gold) using an EMS Q150T ES sputter coater to prevent charging of the polymer during imaging. Images were inspected to see if nanoparticles were properly dispersed.

2.5.2 Thermogravimetric Analysis (TGA)

Thermogravimetric samples were also measured from bulk material of arbitrary size. TGA was performed for many print samples to assess how the nanoparticle content of printed content compared to initial percent loading. A Discovery TGA (TA Instruments, USA), was used.

A 10-day experiment was performed to assess the stability of the magnetic colloid over time. A drop of ink was collected from newly dispersed FEO (RIG-15%FE3O4-10%BYK-5%GEN) for 8 separate days starting one day after fresh formulation. Droplets were taken collected and measured on the first 4 consecutive days. There were two days without measurement, and then measurements resumed for the next 4 consecutive days. The ink

was cured externally from the printer using a UV curing conveyor belt (Fusion UV, USA) and the magnetite concentration was measured via thermogravimetric analysis.

2.5.3 Vibrating Sample Magnetometer (VSM)

A vibrating sample magnetometer (ADE Technologies, USA) was used to obtain the magnetic hysteresis loop of printed magnetic inks. Measurements were made at room temperature. The mass of each sample was recorded.

For RIG-15%FE3O4-10%BYK-5%GEN, a 5 mm x 5 x .035 mm thin square film sample was measured. A 5-mm sample holder was use for the VSM. The mean of the TGA-measured loading of the printed material was 8.7 ± 4.5 wt% (95% confidence interval, n=3).

For RIG-5%COFE2O4-3%BYK-0%GEN, a 10 mm x 10 mm x 0.035 mm thin square film sample was printed using MultiFab. This sample had a TGA-measured mean actual loading of 1.6 ± 1.0 wt% (95% confidence interval, n=3). The sample was loaded into the VSM using an 8-mm sample holder.

2.5.4 Tensile Testing (RIG and ELA)

The magnetic inks were not intended for use as structural material; it was known (and qualitatively observed) that the magnetic inks would cause weaker curing compared to the base inks, resulting in less robust structures. RIG and ELA were used for the structural elements of any prints. As such, mechanical elastic modulus testing was performed to characterize the materials. Testing was performed with an Instron 5944 (Instron, Norwood, MA, USA), a single column table top mechanical testing system. Samples were relatively thin (15 layers, measured as 0.26 mm) to simulate conditions similar to those commonly used in prints. The strain rate was 5 mm/s.

3 Ink Results & Discussion

Results regarding nanoparticle, base ink, and dispersion methods are presented followed by characterization of printed magnetic inks as well as the structural characterization of ELA and RIG.

3.1 Nanoparticle Results

Qualitative results for dispersion with the particles listed in Section 2.1 are described in this section.

3.1.1 PVP-coated Iron Oxide (Fe_3O_4, US Nano)

This sample appeared to have reasonable dispersion in the polymer. There was some difficulty passing the ink through the filter. At 70 °C, the viscosity was measured within the printing range. The sample was jetted from the Jet Xpert, but not reliably. Eventually, channels appeared to be clogged.

3.1.2 Cobalt Iron Oxide ($CoFe_2O_4$, US Nano)

This sample had a viscosity within the printing range. However, after using the viscometer the colloid appeared to have separated, with significant visible settling. The sample was tested in JetXpert, but the clogging was immediately present in the printhead.

3.1.3 Nickel Iron Oxide ($NiFe_2O_4$, US Nano)

This sample visibly separated while passing through the 1-micron filter. It is believed that there was too much agglomeration to allow for proper dispersion.

3.1.4 Iron Oxide (Fe_2O_3, Sigma-Aldrich)

This sample also had viscosity within the printing range, but separation was readily apparent in the ink bottles. Printhead nozzles clogged immediately when the sample was tested in JetXpert.

3.1.5 Cobalt Oxide (Co_3O_4, Sigma-Aldrich)

The ink seemed to pass the filter without significant separation. The simple had viscosity on the high end of the printing range at 70 °C. The ink could be purged through the printhead at high pressures, but did not jet out well.

3.2 Dispersion Method Results

Ultrasonification, being the dispersion method previously used by CFG for nanoparticles ink photopolymers, was used extensively for initial testing. However, as described above, there was limited success with the ultrasonic dispersions.

The industrial immersion blender yielded worse results. It proved difficult to get mixture sufficiently moving. There was significant nanoparticle build-up still present at the bottom of the beaker after processing.

The bead mill mixtures immediately showed more stability than the inks processed with the ultrasonification; the inks were darker, indicating more nanoparticles suspended in the fluid as opposed to settled at the bottom. There was less visible separation when the ink passed through the filter. Lastly, a RIG-2.5%FE3O4-1%BYK-0%GEN ink proved jettable in JetXpert.

Pre-dispersed mixtures did not show promise. Upon arrival, nanoparticles already appeared to be settled. The viscometer measurement failed to give a reading, which is usually due to conductivity of the sample. The dispersion did not seem to clog the printhead during JetXpert testing, but did not successfully jet out. The concentration was diluted by adding additional water, but that did not improve the results.

3.3 Loading and Base Ink Results

Adding nanoparticles increases the viscosity of an ink. As particle loading was increased the viscosity needed to be monitored to ensure that the ink was still within the printing range at the printing temperature of 70 °C. Viscosity results are presented showing how viscosity varies with increased nanoparticle loading as well as how viscosity varies with added wt% of Gen1117, the low viscosity monomer.

3.3.1 Varying Nanoparticle Loading

Figure 3.1 shows a scatterplot of the viscosity of magnetic inks where only added wt% of the nanoparticle (Fe_3O_4) was varied in the ink composition. The viscosity limit of 16 cP is noted on the graph, and it can be seen that increasing the added wt% to 15 caused the viscosity to not cross the threshold into the printable range by the printing temperature. Viscosity for RIG-15%FE304-3%BYK-0%GEN was 16.6 cP.

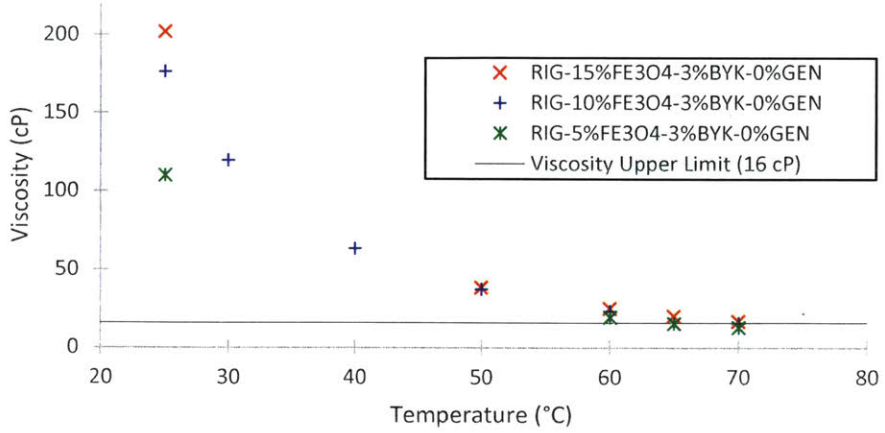

Figure 3.1: Scatterplot of viscosity vs. temperature for 5% (green), 10% (blue), and 15% (red) added weight of nanoparticles. The black line indicates the upper bound of the printing viscosity limit.

3.3.2 Varying Gen1117

Figure 3.2 shows a scatterplot of viscosity of magnetic ink where added wt% of Gen1117, the low viscosity monomer, was varied. Viscosity was measured for added Gen1117 levels at 0 added wt%, 10 added wt%, and 20 added wt%. With 10 added wt% Gen1117, the viscosity at 70 °C crosses into the printing threshold at 14.9 cP. With 20 added wt% Gen1117, the viscosity is 8.17 cP, indicating significant room for increasing loading. However, it should be noted that increasing Gen1117 decreases the expected actual wt% of the of the nanoparticles from 15.0 wt% to 13.6 wt% and 12.5 wt%, for 10 added wt% and 20 added wt% of Gen1117, respectively. Furthermore, Byk110 was at 3 added wt% for Gen1117 at 0 and 10 added wt%, but at 5 added wt% for the 20 added wt% sample, which somewhat limits the conclusions that can be drawn from these results.

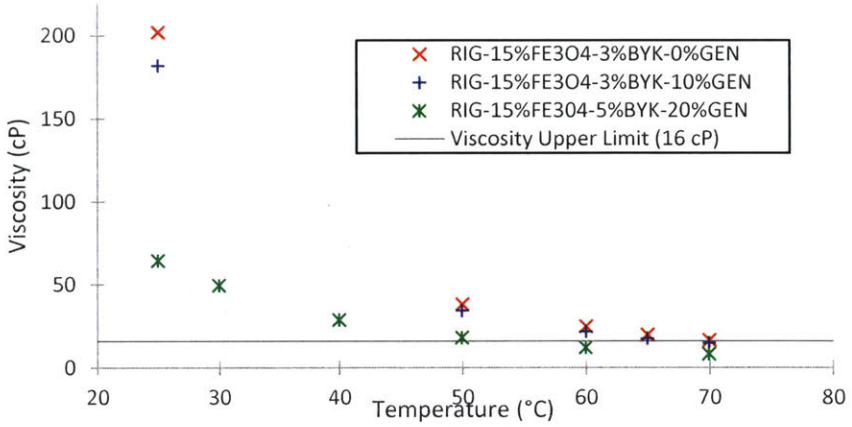

Figure 3.2: Scatterplot of viscosity vs. temperature for 0% (red), 10% (blue), and 20% (green) added weight of Gen1117. The black line indicates the upper bound of the printing viscosity limit.

3.3.3 Varying Base Ink

RIG was the first base ink explored due to the success with hydroxyapatite. It was considered a more ideal candidate than ELA or EPX as a base ink for separate reasons. ELA was considered less desirable because it was designed to have minimally low strength, and would likely be compromised by the introduction of nanoparticles. EPX as a base already has a higher viscosity than RIG, so it did not seem as promising. Thus, ELA and EPX were only briefly explored when loading conditions seemed to be maximized in RIG, and it seemed reasonable to simply verify if either ELA or EPX showed any potential for significantly increased loading of nanoparticles, i.e. lower viscosity at equivalent added wt% concentration levels. Table 2 show viscosities measured with equivalent magnetite content and varying base ink. There was 3 added wt% of BYK110 to both the RIG and ELA, and 5 added wt% of BYK in the EPX.

Table 2: List of inks and viscosities at 25 °C, 60 °C, 65 °C, and 70 °C. Values highlighted in red indicate that the viscosity at printing temperature is out of printable range.

	Viscosity (cP)			
Nanoparticle	**25 °C**	**60 °C**	**65 °C**	**70 °C (printing temperature)**
RIG-10%FE3O4-3%BYK-0%GEN	148.5	20.3	16.3	13.4
ELA-10%FE3O4-3%BYK-0%GEN	191.6	24.4	19.5	16.1

EPX-10%FE3O4-5%BYK-0%GEN	208.0	22	19.6	16.2

3.4 Discussion

This section draws conclusions from the subsections of results presented above.

3.4.1 Nanoparticles

Only the PVP-coated iron oxide nanoparticles jetted to any significant degree when ultrasonically dispersed. This nanoparticle became the primary candidate for future experimentation. One known drawback about this nanoparticle is that it has very low remanence and coercivity, despite higher mass magnetization, limiting potential applications for future structures. Because the reported remanence and coercivity of the cobalt iron oxide nanoparticles were significantly higher than the PVP-coated iron oxide, this nanoparticle was also selected for additional experimentation.

3.4.2 Dispersion Method

Even qualitative results were enough to show that the dispersion created via the bead mill were the most successful. It was important to see decreased settling and separation of the nanoparticle in the bottle and during filtration. Most importantly, creation of the first reliably jettable ink in JetXpert led to the bead mill being chosen as the dispersion method moving forward. One drawback of this method is that it requires a full work day of processing, limiting the turnaround time for experimentation. A drawback shared by the ultrasonicator, blender, and bead mill is that they require a minimum liquid amount of approximately 100 mL, imposing high costs for testing, especially with high loading of nanoparticles.

3.4.3 Base Ink and Loading

Naturally, the higher the loading of nanoparticles, the higher the forces that can be achieved, and the more versatile the actuators can be. Even 15 wt% corresponds to just 3% volume for magnetite, which means there is significant room for improvement. It is clear that there is potential for increased proportion of low viscosity monomers (i.e. Gen1117) in the base ink to combat the increased viscosity due to increased nanoparticle loading. However, the effectiveness of this method for bringing a viscosity for a certain ink loading within printable range is inherently limited in that adding more of the constituents

decreases the final wt% that is possible for the magnetic nanoparticle. It is not believed that the absolute maximum stable wt% loading for nanoparticles was achieved in this work, but that the maximum practical loading for inkjet printing is not far from the 15 added wt% results due to other printing difficulties concomitant with higher loading (see next Section). Fortunately, significant actuations are already achievable at this concentration, especially when the multi-material context is exploited.

3.5 Test Prints and Material Characterization Results

Preliminary prints, made primarily with magnetite inks, allowed for a physical understanding of what might be enabled with this printing technology, while additional measurements provided additional data needed for more formal characterization of the material. The tested magnetic ink was RIG-15%FE304-5%BYK-10%GEN unless otherwise noted.

3.5.1 Test Prints

Initial prints showed homogeneous dispersion of the nanoparticles. Observation with an optical microscope did not reveal any nanoparticle clusters. Figure 3.3 shows opacity of the material increasing as layers are added to the print. Each layer has a thickness of approximately 18 microns, similar to that of a plain RIG print and showed no decreased surface quality compared to RIG prints.

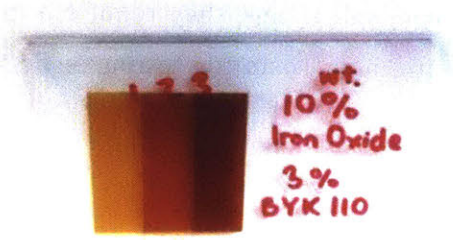

Figure 3.3: Photograph of 30x30 mm print on a glass slide showing opacity increasing as the layer height of the print is increased left to right from 1 layer to 3 layers.

A 1.5 in. x 0.25 in. x 0.25 in. N42 nickel-plated neodymium magnet (K&J Magnetics, USA) was used to pick up printed samples, and then bend thin (10-layer) samples. Figure 3.4 shows screenshots of two videos of the samples with and without the presence of a magnet, demonstrating magnetic actuation potential.

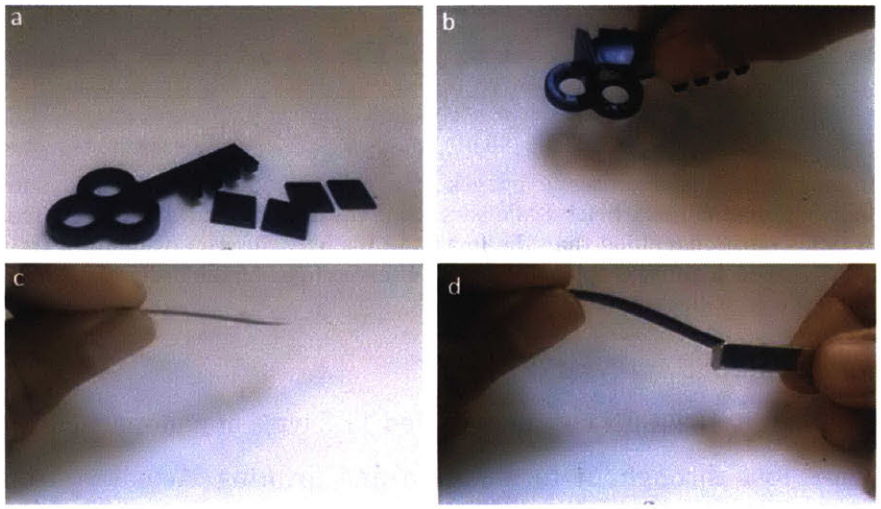

Figure 3.4: Screenshots of videos taken to demonstrate the magnetic actuation potential of magnetic inks. In one video, several printed objects (**a**) are picked up by the magnet (**b**). In the other video, a thin sample (**c**) is bent by the presence of the magnet (**d**).

One notable issue was that as added weight percent of the magnetite particles was increased to 20 added wt%, the print material failed to fully cure. This caused the print to be more gel-like than solid, which would not be robust enough for most printed structures, especially given that most of the proposed applications for the structures are dynamic. For this reason, concentration of the magnetite particles was capped at 15 added wt%, with the specific formulation being RIG-15%FE304-5%BYK-10%GEN.

3.5.2 Scanning Electron Microscope (SEM)

Figure 3.5 shows results from the SEM at two different zoom levels. The magnetite particles (lighter specks in the images) appear well-distributed in the printed material. The individual specks seem spherical and their diameter appears to correspond with that of a single magnetite particle (15-30 nm), a positive indication of a lack of agglomeration.

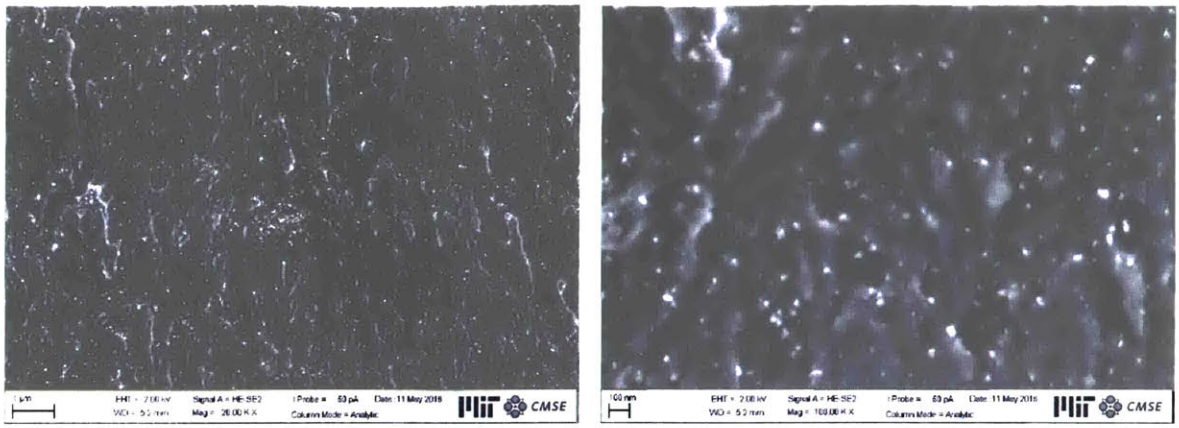

Figure 3.5: Scanning electronic microscope images of a gold-coated printed sample shows relatively homogeneous distribution of nanoparticles. Scale bars are in the lower left corner of each image; the image on the right is 5 times more magnified than the image on the left. The iron oxide appears as the lighter specks in the images and each entity is spherical and is observed to be on the order of a single nanoparticle (~20 nm), indicating a lack of clusters.

3.5.3 Thermogravimetric Analysis (TGA)

RIG-15%FE304-5%BYK-10%GEN has an expected 11.2 wt% of nanoparticles in the print if no particles were lost throughout formulation and printing. Actual concentration was measured as 9.7 ± 0.8 wt% (95% confidence interval, n=43) via TGA, showing that a statistically significant percent of the nanoparticles do not in fact make it to the final print, but that a large majority do.

TGA measurements were also made from RIG-10%COFE2O4-5%BYK-20%GEN sample prints, which have an expected concentration of 7.2 wt%. The measured concentration of cobalt iron oxide nanoparticles was 2.3 ± 0.2 wt%, showing that a majority of the nanoparticles settled out of the material during formulation or before printing. This low concentration translated to a low amount of achievable magnetization of prints.

Lastly, Figure 3.6 shows the results of the mean TGA-measured nanoparticle concentration across the 10-day experiment. The mean of the TGA-measured means of the first four days, 9.0 ± 0.5 wt% was not statistically significantly different from that of the last four days, 8.8 ± 0.5 wt%. Thus, the ink can be considered stable for at least 10 days and potentially longer. It is not known why the standard deviation of measurements from the first four days varied more than that of measurements from the last four days.

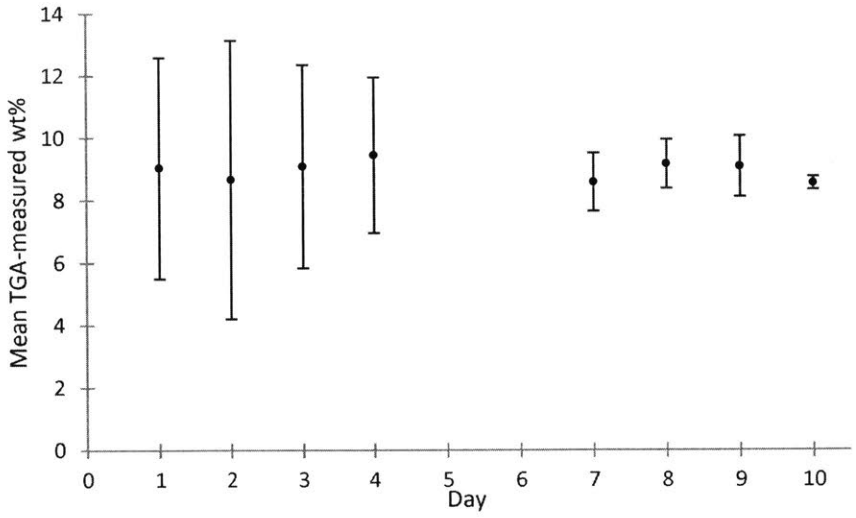

Figure 3.6: Mean TGA-measured wt% of samples drawn from the same ink bottle over 10 days is plotted. Error bars are based on a 95% confidence interval with n=3 for all days.

3.5.4 Vibrating Sample Magnetometer (VSM)

Figure 3.7 show the B-H curve for the RIG-15%FE3O4-10%BYK-5%GEN sample. The saturation mass magnetization, M_S, is 46.6 emu/g, which for all practical purposes matches the value reported by US Nano, 60.5 emu/g. Similarly, hysteresis is barely observable and the coercivity and remanence are virtually 0, indicating that the nanoparticles are indeed very soft magnets at room temperature.

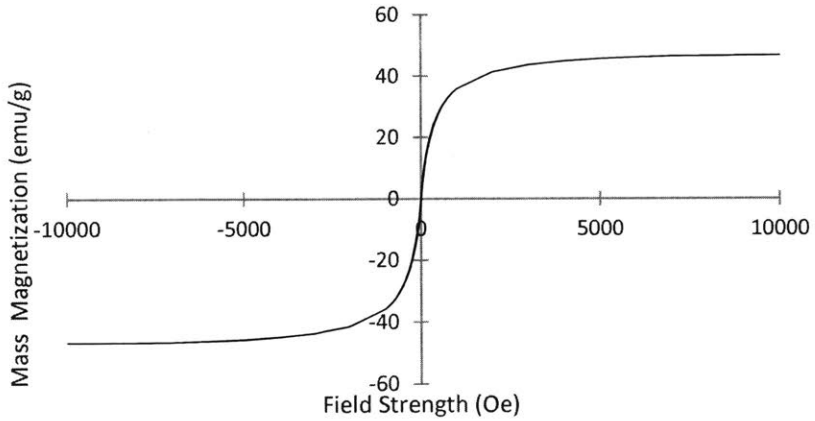

Figure 3.7: B-H (hysteresis) curve for PVP-coated magnetite measured from a printed sample.

For cobalt iron oxide, coercivity was report to be 900 Oe, but the measured value was 160 Oe. . This is an order of magnitude higher than the value measured for magnetite, but still lower than the coercivity of magnetic materials used in temporary magnetic strip cards. Thus, its use for information storage is possible, but fairly limited. Saturation mass magnetization and magnetic remanence were measured as 66.3 emu/g and 13.0 emu/g, respectively. These, once again, are reasonable compared to the reported values of 46.8 emu/g and 17.3 emu/g. The hysteresis loop measured from the sample of RIG-5%COFE2O4-3%BYK-0%GEN is shown in Figure 3.8. It is notably wider than that of the magnetite sample, but is still relatively soft.

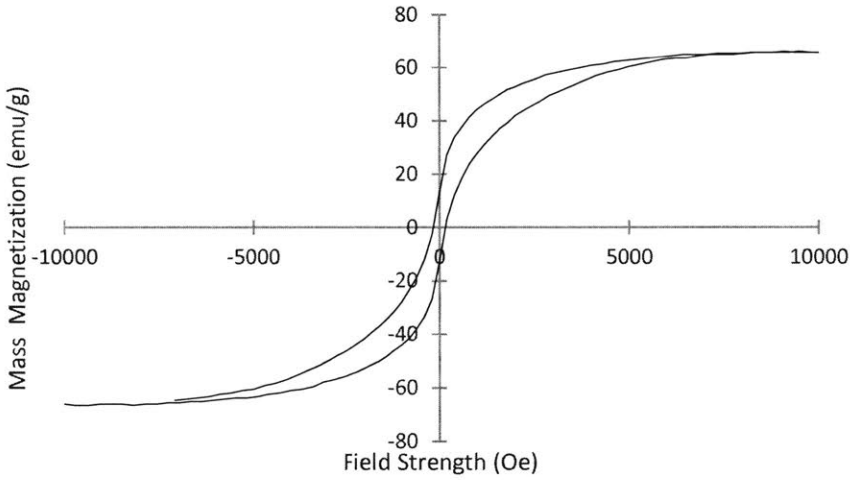

Figure 3.8: B-H (hysteresis) curve for cobalt-iron oxide from a printed sample.

3.5.5 Tensile Testing

The elastic modulus for RIG was measured up to 0.05 strain as 570 ± 70 MPa (95% confidence interval for n=3). Full data from the tests can be seen on the left side of Figure 3.9.

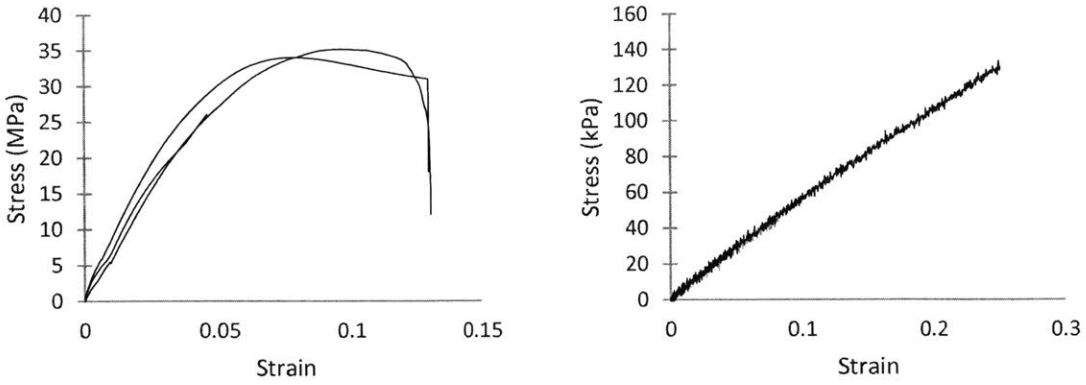

Figure 3.9: Tensile test results for 3 thin samples of RIG (left) and 3 samples of ELA (right). The ELA data does not include the breaking of the sample.

The elastic modulus for ELA was 570 ± 30 kPa. Full data from the tests can be seen on the right side of Figure 3.9. The data from all three tests was in nearly perfect agreement such that the results overlap. Data collection was stopped before the samples broke.

3.6 Suggestions for Future Work in Ink Development

This section provides suggestions for future work specifically related to magnetic ink development.

3.6.1 Particle Type

The referenced materials show a very wide range of applications that are achievable with magnetic actuators. Many of these actuators operate based on magnetic torque felt in a constant field rather than in a field with a gradient. This is at odds with inkjet 3D printing because rod-like particles would be more ideal to fix anisotropy in a print, but the spherical particle are desirable to prevent clogging. Magnetite is an extremely soft magnet which limits the scope of possible applications for this new magnetic material. It would be desirable to not only increase the magnetization of the print material, but also to print something that can be called a magnet rather than simply magnetic.

As shown in Section 3.5.4, the cobalt iron oxide nanoparticle has stronger magnetic properties than the iron oxide and therefore a wider range of potential applications. This particle was not pursued for this work due to the apparent dispersions issues. However, these dispersion issues could likely be overcome with more base ink or dispersant experimentation.

Some materials, like the cobalt iron oxide, were cost-prohibitive for extensive testing when ordered from material suppliers. However, a number of the referenced materials used in-lab nanoparticle synthesis methods that are significantly more cost-effective. The cost will become even more important as higher nanoparticle concentration loadings and larger prints and applications are explored.

3.6.2 Base Ink Type

RIG was chosen over ELA and EPX because it showed more initial promise for enabling higher loading of nanoparticles. It would be interesting to explore other carriers for a few reasons. Dispersion in ELA is particularly interesting because fully soft actuators could be printed. Dispersion in other materials in general is important to ensure more seamless interfaces between magnetic and non-magnetic areas in a print.

On a different note, an important base ink type would be the development of one that can be precipitated away by a heater or some other process as is done for 3D printed conductive traces. This would allow for printing of areas that are fully populated with magnetic material, which would allow a many-fold increase over the currently achievable forces for a given volume.

3.6.3 Particle Loading

As discussed previously, the method of decreasing viscosity by increasing the proportion of low viscosity monomers inherently limits the maximum possible nanoparticle loading. The magnetic content in inks presented here are very far from pure magnetic materials, which could deter use of this new manufacturing method in favor of existing techniques, even if they are less streamlined. For this work, it was too cost prohibitive to try the full range of particle loadings and ink constituent variations to achieve the absolute maximum percent weight of the nanoparticles. However, cheaper in-lab synthesis methods could change the material costs drastically, opening opportunity for more extensive exploration. The cobalt iron oxide maximum concentration could be improved significantly from the presented results.

4 Design of Structures

Because this work involved printing with a novel magnetic ink in a multi-material context, it was deemed critical to characterize actuations that could be achieved with simple structures. The hope is that the results from this work can be used as the building blocks for more complex designs, though several functional applications can be drawn even from the simple structures featured here.

The two primary structures discussed here are a fixed cantilever (Section 4.1) and a tilting panel (Section 4.2). The cantilever has an RIG body and a small block of FEO on one end used to create deflection forces. The tilting panel, half RIG and half FEO, is attached to a frame via thin flexible hinges made of ELA. While the cantilever was used purely for characterization and validation purpose, creating arrays of the tilting panel and adding other features showed the structure's versatility to be used in a number of applications. In Section 4.3, additional print structures are discussed from a more qualitative perspective.

4.1 Fixed Cantilever

The fixed cantilever was chosen as a simple structure to feature both RIG, with measured mechanical properties (see Section 3.5.5), and FEO, with measured magnetic properties (see Section 3.5.4). Multiple copies were made while varying cantilever thickness, t_{RIG}, or block thickness, t_{FEO} (see Figure 4.1), and holding all other design parameters constant. During testing, the cantilever length, l_{RIG}, was also a variable; it was adjusted by changing the clamping location. Deflection of the cantilevers was measured in the presence of a magnet; the procedure for these measurements is described in Section 4.1.3. These results are compared to an iterative first order magnet and structural model in Section 5.3.2 using the measurements of the structural and magnetic properties of the involved materials as inputs. The physical set-up of the measurements and experimental procedure are further detailed below.

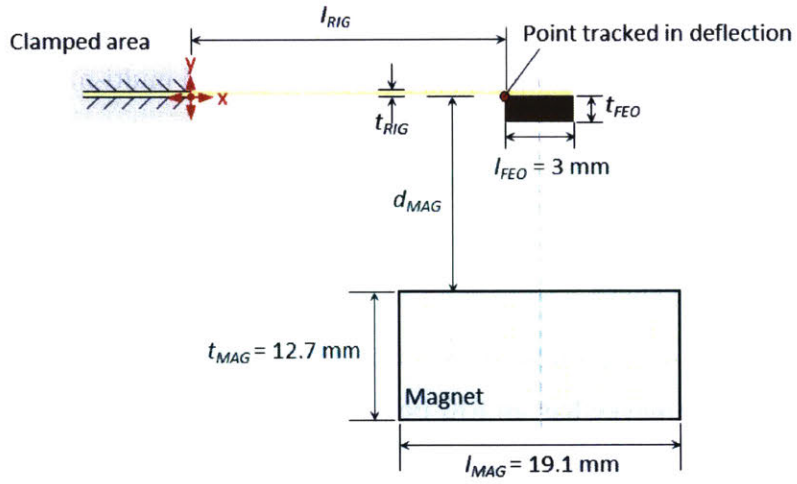

Figure 4.1: 2D schematic of cantilever and measurement set-up. The origin and the point tracked in deflection measurements are noted. Dimensions are listed for parameters that did not change during testing. The out-of-plane dimension for the cantilever and FE FEO block is 3 mm. The out-of-plane dimensions for the magnet is 19.1 mm. The FEO block is centered above the magnet in X and Z.

4.1.1 Varied Parameters

The structure is a simple cantilever with a fixed end and a magnetite ink (FEO) block on the end. The out-of-plane dimension (Figure 4.1) for the cantilever and FEO block is 3 mm and is not varied. The FEO block is square and only its thickness, t_{FEO}, is varied. The thickness of the FEO block, t_{FEO}, was also varied. The length of the cantilever, l_{RIG}, was varied by clamping the cantilever at a different location along its length. The clamping location determines the origin of the measurement, with the X-direction being along the length of the cantilever and Y-direction being the primary direction of deflection. Gravity was in the Z-direction and is neglected. A total of 5 different cantilever geometries were printed. t_{FEO} was input as either 0.525 mm, 0.875 mm, or 1.225 mm, which corresponds with 30, 50, or 70 printed layers, respectively. t_{RIG} was either 0.105 mm, 0.175 mm, or 0.245 mm, which corresponding with 6, 10, or 14 layers, respectively. During clamping, l_{RIG} was set at approximately either 11 mm or 15 mm. The actual dimensions for each cantilever were measured during tested using calipers. The input dimensions of each of the 10 unique cantilevers are noted in Table 3. Each cantilever is numbered for sake of future reference.

Table 3: Input dimensions for printed cantilevers. All dimensions are in millimeters.

Cantilever	l_{RIG}	t_{RIG}	t_{FEO}
1	11	0.105	0.525
2	11	0.105	0.875
3	11	0.105	1.225
4	11	0.175	1.225
5	11	0.245	1.225
6	15	0.105	0.525
7	15	0.105	0.875
8	15	0.105	1.225
9	15	0.175	1.225
10	15	0.245	1.225

4.1.2 Printing Procedure

The cantilever actuators were modeled in SolidWorks, with distinct parts created for the RIG cantilevers and FEO blocks. All cantilevers were included in a single assembly. The assembly was output as two .STL files, one containing all of the cantilever (RIG) parts, and the other containing the FEO blocks. The .STL was voxelized and assigned the appropriate materials and brought into Fabricator. RIG and RIG-15%FE3O4-5%BYK-15%GEN were loaded into the printer after filtering the inks and vacuuming the bottles to remove air bubbles. Two glass slides were used as a substrate for the print.

4.1.3 Cantilever Deflection Measurement

A cuboidal neodymium N52 magnet (0.75 in. x 0.75 in. x 0.5 in., K&J Magnetics, USA) was fixed to a ¼-inch manual linear translation stage (Thorlabs, USA) using plastic screws and a 3-mm plate of acrylic. Each cantilever was sequentially loaded into a clamp. The magnet was placed in relation to each cantilever as shown in Figure 4.1, with the FEO block centered in X and Z in front of the square face of the magnet. Geometries were measured using calipers. A camera was mounted above the set-up to capture the same view shown in the schematic. A calibration pattern was included in the field of view on the plane of the top

face of the cantilever and FEO block. The length of the cantilever was moved parallel to the magnet until a deflection could be observed. From there, the linear stage was moved in 0.05 in. increments, allowing time for the cantilever to reach a static equilibrium and for a photo to be taken at each state. Measurement was completed when the linear stage reached its maximum range or if the cantilever was drawn in far enough to collide with the acrylic plate that held the magnet.

The photographs were brought into Logger Pro 3.10.1 (Vernier Software & Technologies, USA). The photo analysis tool was used to calibrate the images and obtain measurements tracking the deflection of a point on the cantilever as the distance of the magnet from the cantilever varied. Figure 4.2 shows a sample set of images used to obtain deflection measurements, overlaid to show the different positions of the cantilever as the field was changed.

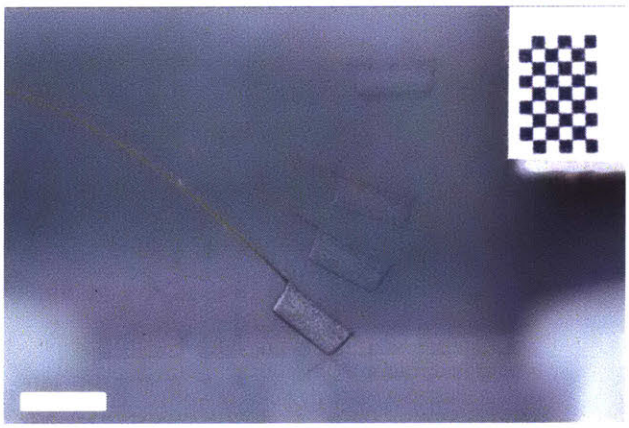

Figure 4.2: Sample overlay of photographs used for cantilever deflection measurement. Scale bar is 3 mm.

4.1.4 Magnetic Field Measurement

The magnetic field measurement set-up was similar to that of cantilever measurement, but with a new origin for measurements centered on the magnet face perpendicular to the direction of magnetization. The F. W. Bell 9500 gaussmeter's probe was fixed in X and Z in front of the magnet, while the linear stage, moving in the Z-direction, was adjusted in 0.05 in. increments. The corresponding gaussmeter measurements were recorded at each position. Measurement was made in the 3 KG range, which has a reported accuracy of ± 30

Gauss. Fields of various magnets were recorded. Figure 4.3 shows the measurement set-up for a 1.5 in. x 0.25 in. x 0.25 in. N42 nickel-plated neodymium magnet. The X- and Z-position of the probe tip with respect to the magnet was noted. In the photograph, the probe tip is located at X = 0 and Z = 0.

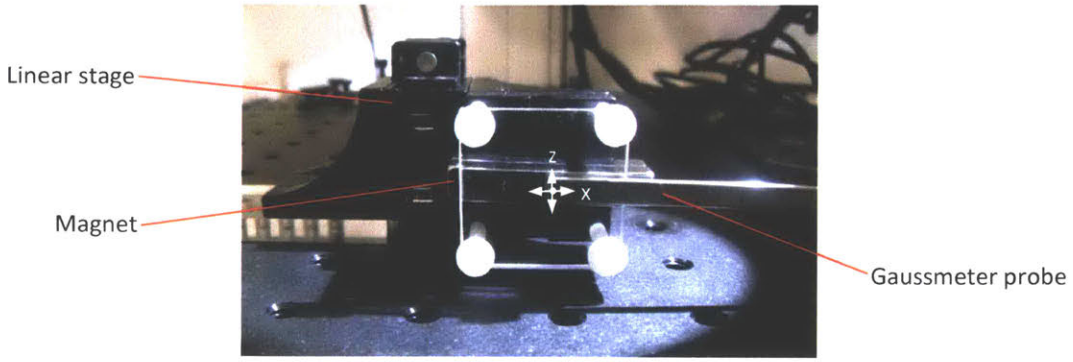

Figure 4.3: Photograph of magnetic field measurement set-up. The magnet measured in the photograph is a 1.5 in. x 0.25 in. x 0.25 in. N42 nickel-plated neodymium magnet (K&J Magnetics).

4.2 Tilting Panel

A broad range of applications are proposed based on the tiling of a simple structure, a tilting panel. Figure 4.4 shows labelled views of a single tilting panel and frame. Broadly, the structure is a panel that is half RIG and half FEO (or a combination of FEO and RIG) and connected to the frame via flexible ELA joints. There are some nuances in the structure's design that can, for example, ease part removal after printing and improve robustness of the results. Geometries were selected to maximize the area of the panel with respect to the frame, which is desirable for most applications because they depend on the panel behavior and not the frame behavior. However, for testing, the frame was imbedded in a larger body of RIG (not shown). Features were also driven by the intention to maximize possible deflections. The printing procedure was unchanged from Section 4.1, aside from starting with a different SolidWorks model and introducing ELA as a third material (requiring a third .STL input file for Fabricator). Magnetic field measurements were reused from the earlier tests.

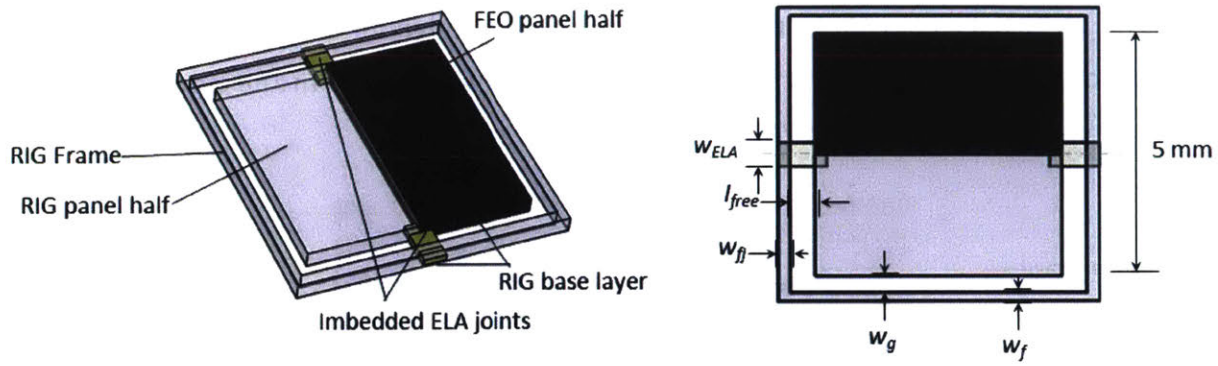

Figure 4.4: SolidWorks screen captures with labelled elements of the square panel and frame (left) and parameters indicated on a top view of the model (right). Out-of-plane parameters (not indicated) are the thickness of the panel and the ELA joints.

The square panel is 5 mm x 5 mm and divided into two halves. One half is entirely RIG. The other half is designed to be a combination of FEO and RIG, assigned based on desired tilting angle of the panel. An exception is that the first layer of the whole panel is RIG, which enables easier separation from the print substrate. As such, the total thickness of the panel is the thickness of the FEO side, t_{FEO}, plus the thickness of one layer of RIG, 0.0175 mm.

The ELA joint ends are imbedded 0.25 mm into both the frame and the panel and have 0.5 mm free length, l_{free}, for a total of 1 mm in length. The thickness, t_{ELA}, can vary. The width, w_{ELA}, was fixed at 0.5 mm, the smallest reliably printed width for ELA. Where the joint is imbedded in the frame, the base layer is RIG, facilitating part removal in addition to fully constraining the end of the joint.

The spacing between the panel and the frame was minimized. On two sides this is determined by the ELA joint free length, but on the other side this is determined by calculating the gap necessary such that the panel does not collide with the frame when tilting. This gap width, w_g, was 0.35 mm, which is close to the minimum gap width required by the printer to ensure distinct parts. The minimal frame width, w_f, was 0.15 mm, such that when the full structure was tilted, the total frame width was 0.3 mm, the smallest reliably printed width for RIG. However, the frame width in the other direction, w_{fj}, was the same length as the ELA joint ends, or 0.25 mm, for a total frame with of 0.5mm.

4.2.1 *Varied Parameters*

The two varied parameters in testing were joint thickness, t_{ELA}, and FEO thickness, t_{FEO}. Based on preliminary tests, the minimum thickness for the ELA joint was 0.0175. Thus, three values selected for t_{ELA} were 0.175 mm (10 layers), 0.210 mm (12 layers), and 0.245 mm (14 layers). Three values selected for t_{FEO} were 0.3325 mm (19 layers), 0.5075 mm (29 layers), and 0.6825 mm (39 layers). Three copies of all of the unique combinations of the panels were printed. The nine combinations are summarized in Table 4. The panels are numbered for future reference.

Table 4: Input dimensions for printed panels for tilt measurements. All dimensions are in millimeters.

Panel	t_{ELA}	t_{FEO}
1	0.175	0. 6825
2	0.210	0. 6825
3	0.245	0. 6825
4	0.175	0. 5075
5	0.210	0. 5075
6	0.245	0. 5075
7	0.175	0.3325
8	0.210	0.3325
9	0.245	0.3325

4.2.2 *Panel Tilt Measurement*

The bottom surface of the print is conveniently reflective, which allows measurement of angle measurement using laser pointer and trigonometry. Figure 4.5 is a simplified schematic showing the measurement set-up for the tilting panel tile measurements. The print was mounted into a clamp and then mounted perpendicular to the laser pointer. The magnet distance, d_{mag}, was adjusted and measured at three different stages: Case 1) when the reflected laser was 0.5 m from the starting position; Case 2) when the reflected laser was 1 m from the starting position; and Case 3) when the laser reflected perpendicular to the starting angle, indicating that the panel was tilted at 45°. Through consistent measurement of d_{mag} and d_{wall}, the distance from the magnet surface to the wall, the angles

corresponding to Cases 1 and 2 are calculated to be effectively 16 and 25 degrees of tilt, respectively.

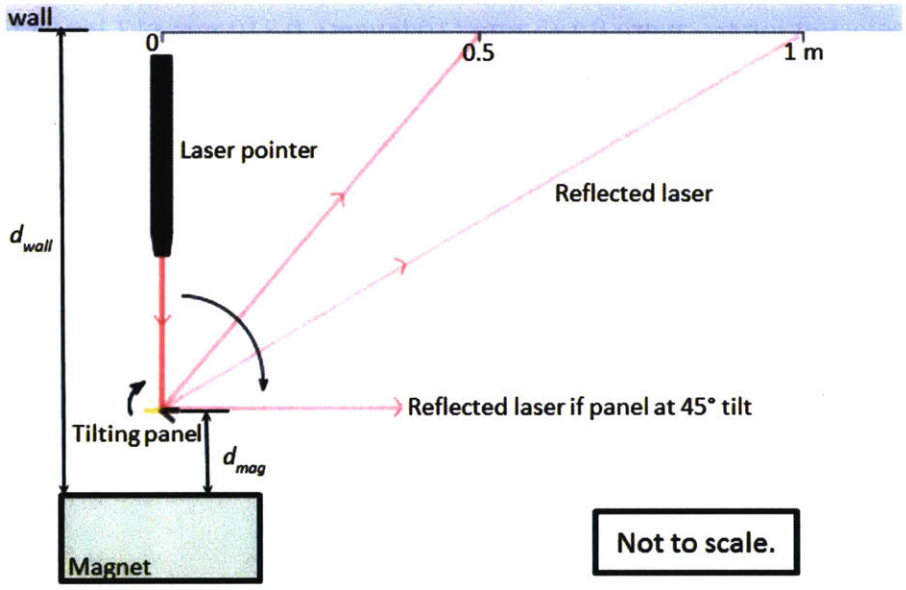

Figure 4.5: Schematic of the panel tilt measurement set-up. The laser point reflects off the surface of the panel. The distance from the magnet to the panel was measured using calipers.

The magnet use for measurement was a cuboidal neodymium N52 magnet (0.75 in. x 0.75 in. x 0.5 in., K&J Magnetics, USA). The three measurements were performed once for each panel, obtaining three sets of measurements for each panel geometry due to having three copies of each geometry.

4.3 Additional Printed Structures

After the preliminary prints and the validation prints, some more advanced configurations were explored.

4.3.1 Functional Panel Arrays

One tilting panel, even if finely controlled, is limited in terms of its potential for use in functional applications. However, Figure 4.6 shows how a single panel and frame can be tiled to form a paneled surface. Resizing and making small variations to the panels can lead to a wide variety of interesting panel arrays with functions that remain hidden unless in the presence of a magnetic field. One of the strength of 3D printing is that it enables the fabrication of large arrays of uniquely-tuned panels with relative ease.

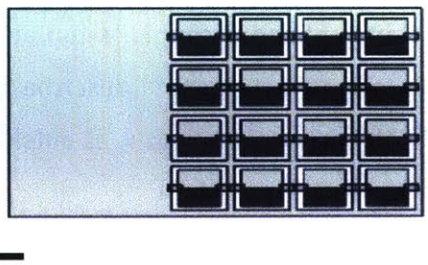

Figure 4.6: Top view of SolidWorks model of a 4 x 4 tiled array of 3 mm x 3 mm panels. Scale bar is 5 mm.

4.3.2 Double-Tilting Panels

Many of the applications that benefit from fine control of panels that tilt on a single axis can further benefit from extension of the method to two axes. By imbedding the frame of a single panel into another thin frame with joints on the opposite axis, two directions of tilt can be controlled. Figure 4.7 shows a 2 x 2 array of double-tilting panels in its flat, i.e. printed, configuration. The FEO was manually placed such that the innermost corner of each panel would be drawn in the most by the magnet, such that the panels would form a concave structure.

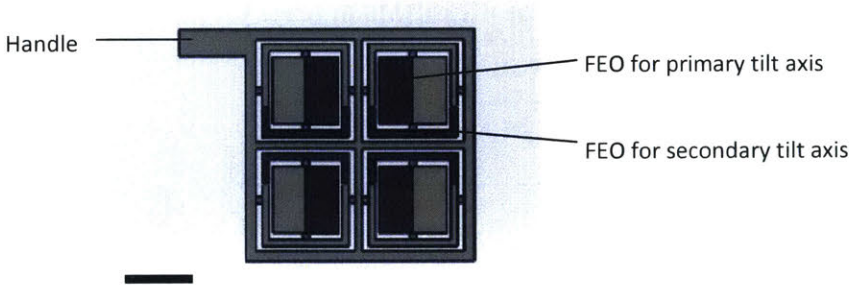

Figure 4.7: Top view of SolidWorks model of print for a 2 x 2 array of double-tilting panels.

5 Theoretical Modeling of Actuators

The actuators span two domains, structural and magnetic. There is an inaction between the two in that the forces that move the actuators are dependent on the magnetic material's position in the field. Two actuators, a cantilever and a tilting panel, were evaluated with theoretical models. The magnetic field and body force equations are relevant to both actuators.

5.1 Magnetic Field

Consider a rectangular magnet magnetized through its top and bottom faces, which have dimensions $2a$ and $2b$. The following equations[49] describe the three components of a magnetic field intensity (H_X, H_Y, H_Z) at a point P=(x, y, z) outside a magnet, with the origin located at the center of the top face (see Figure 5.1):

$$H_X = \frac{J}{2\mu_0}\ln\left[\frac{y+b+\{(y+b)^2+(x-a)^2+z^2\}^{1/2}}{y-b+\{(y-b)^2+(x-a)^2+z^2\}^{1/2}} \times \frac{y-b+\{(y-b)^2+(x+a)^2+z^2\}^{1/2}}{y+b+\{(y+b)^2+(x+a)^2+z^2\}^{1/2}}\right], \tag{5}$$

$$H_Y = \frac{J}{2\mu_0}\ln\left[\frac{x+a+\{(y-b)^2+(x+a)^2+z^2\}^{1/2}}{x-a+\{(y-b)^2+(x-a)^2+z^2\}^{1/2}} \times \frac{x-a+\{(y+b)^2+(x-a)^2+z^2\}^{1/2}}{x+a+\{(y+b)^2+(x+a)^2+z^2\}^{1/2}}\right], \tag{6}$$

$$H_Z = \frac{J}{2\mu_0}\left[\tan^{-1}\left(\frac{(x+a)(y+b)}{z\{(x+a)^2+(y+b)^2+z^2\}^{1/2}}\right) + \tan^{-1}\left(\frac{(x-a)(y-b)}{z\{(x-a)^2+(y+b)^2+z^2\}^{1/2}}\right) - \tan^{-1}\left(\frac{(x+a)(y-b)}{z\{(x+a)^2+(y-b)^2+z^2\}^{1/2}}\right) - \tan^{-1}\left(\frac{(x-a)(y+b)}{z\{(x-a)^2+(y+b)^2+z^2\}^{1/2}}\right)\right], \tag{7}$$

where μ_0 is the magnetic constant equivalent to $4\pi \cdot 10^{-7}$ $T \cdot m \cdot A^{-1}$, and J is magnetic polarization measured in Tesla, assumed to be uniform for the magnet surface. Setting the X- and Y-values to 0, a curve can be generated for the magnetic field as a function of Z, centered above the magnet. This curve is fitted to measured values in Section 6.1. The field

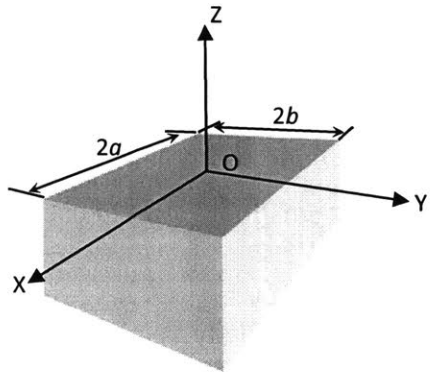

Figure 5.1: Coordinate system and relevant dimensions for analytic magnetic field equations.

intensity from the equations is given in Amperes per meter, but is reported in Gauss to allow for comparison in the measurement units with the conversion equation 1 Gauss = $10^3/(4\pi)$ Amperes per meter.

5.2 Magnetic Body Force

The force, $d\vec{F}$, felt by an infinitesimal element, dV, of a magnetic material in a magnetic field with strength $\vec{H}$ is given by[50]

$$d\vec{F} = \mu_0 \nabla(\vec{M} \cdot \vec{H}), \tag{8}$$

where $\vec{M}$ is the magnetization of the element. Therefore, the total force, F_b, acting on a magnetic body is given by

$$\overrightarrow{F_b} = \int_V d\vec{F} \cdot dV. \tag{9}$$

It should be noted, however, that the magnetic material makes up only a small percentage of the total volume. TGA can be used to measure the weight percent of the magnetic

nanoparticles, $wt\%_{MNP}$, in the printed magnetic material, and this can be converted to a volume percent, $vol\%_{MNP}$, with the following equation:

$$vol\%_{MNP} = \left(1 + \frac{(1 - wt\%_{MNP})}{wt\%_{MNP}} \cdot \frac{\rho_{MNP}}{\rho_{ink}}\right)^{-1}, \tag{10}$$

ρ_{MNP} and ρ_{ink} are the densities of the nanoparticles and the ink, respectively.

5.3 Fixed Cantilever

A few estimates and assumptions are made to implement a first-order iterative model for the specific case of the cantilever. The coordinate system used here is that of the cantilever measurement set-up in Figure 4.1.

First, the FEO block is assumed to be perfectly rectilinear such that the volume of the nanoparticles, V_{MNP}, can be described by

$$V_{MNP} = vol\%_{MNP} \times t_{FEO} w_{FEO} l_{FEO}, \tag{11}$$

where t_{FEO}, w_{FEO}, and l_{FEO}, are the thickness, width, and length dimensions of the FEO block, respectively. Second, in sufficiently high fields, $\vec{M}$ can be estimated as the saturation magnetization, M_S.

Given that the FEO is placed centrally above the magnet, the gradient of the magnetic field in X and Z are estimated as 0. The first-order approximation of the gradient, H_{grad}, becomes

$$H_{grad} = \frac{H_Z(y_p + t_{FEO}) - H_Z(y_p)}{t_{FEO}}, \tag{12}$$

where y_p is the y-coordinate at the tracked deflection point.

Finally, using these approximations, Equations 8 and 9 for the cantilever actuator can be combined and simplified to

$$F_b = \mu_0 V_{MNP} M_S H_{grad}, \tag{13}$$

where F_b is used as the input force for the structural model.

5.3.1 *Magnetic Body Force*

Using small deflection theory[51], the deflection of the free end of a cantilever, δ, acted on by a concentrated load, F, at its tip is given by

$$\delta = \frac{FL^3}{3EI}, \tag{14}$$

where L, E, and I are the length, tensile modulus, and bending moment of inertia for the beam, respectively. The moment of inertia for a rectangular cross-section is

$$I = \frac{bh^3}{12}, \tag{15}$$

where b and h are the width and height of the rectangle, respectively. The parameters correspond with w_{RIG} and t_{RIG}, respectively, for this work.

Use of Equation 15 assumes the measured deflection point to be the effective end of the cantilever, with the body force load acting on it.

5.3.2 *Iterative MATLAB Implementation*

An initial magnetic field gradient can cause the cantilever to deflect. This, in turn, brings the FEO block closer to the magnet where there is a higher field gradient, causing more deflection. This interaction of fields either leads to an equilibrium where the forces cause by the field gradient match the deflection forces, or will cause the FEO block to be completely drawn in, colliding with the magnet, or in this case, the thin acrylic plate in front of the magnet. MATLAB was used to estimate the deflection of the cantilever given the distance of the magnet from its surface.

Without the presence of a magnetic field, y_p, the Y-coordinate of the tracked point, is 0. This becomes the initial condition for y_p and is applied in Equations 12 and then 13 to estimate the body force, F_b. F_b is used in Equation 14 to determine the deflection, which becomes the new y_p. The deflection is iterated upon until it converges or reaches a Y-position that indicates collision with the magnet. Convergence for this model is defined as the previous y_p being within 10^{-9} m of the current y_p. The code for this implementation is provided in Appendix B: MATLAB Code.

5.3.3 Limitations of Model

Some assumptions for the model were described above. Most notably, the deflection equation is for small deformations, and the deformation of the cantilevers routinely goes beyond that. The equations assume that the block remains centrally above the magnet and parallel to it. Because of the large deflections, the block eventually moves a significant distance from the center, which leads to less accurate geometry estimates as well as unaccounted lateral forces in the X-direction due to the introduction of a non-zero gradient. The model also assumes magnetic transparency of all components besides the magnet and the nanoparticles. In short, the model can serve as a first-order estimate, but not much more.

5.4 Tilting Panel

Unlike the cantilever model, the mechanics of the tilting panel are based on torsion equations. This time, "deflection", θ, of a shaft, in this case the ELA joint, is measured in radians and is given by the equation[51]

$$\theta = \frac{T \cdot l}{GJ}, \tag{16}$$

where T is the applied torque, l is the free length of the shaft, G is the shear modulus, and J is the torsion constant. Equation 16 is fairly analogous to the deflection equation, Equation 14, in terms of required parameters. However, the shear modulus and the torsion constant are not as readily obtained as their beam deflection counterparts, modulus of elasticity and moment of inertia, respectively. The shear modulus of the material under torsion in the experiment, ELA, is unknown. Additionally, the experimental geometries are such that the torsion constant is not accurately defined. Visual warping of the joint cross-section during test experiments indicates that conditions for use of a simple linear elastic model are significantly violated. There are additional concerns introduced due to ELA being an extremely soft material.

For these reasons, and based on the predictability of the magnetic inks demonstrated in the cantilever results (see Section 6.2.4), a very different approach for model characterization is used for the tilting panels. As described in Section 4.2.2, measurements were collected regarding tilt angle with a known magnetic field gradient. However, rather than comparing

these results to predicted values, the values are collected to inform an FEM simulation of the tilting panels specially developed in concurrence with this work. The simulation is paired with a topology optimizer that gives users a way to input design specifications and receive an optimized material layout as an output. The optimizer and simulator for the program related to this work were developed by Melina Skouras, who at the time of writing is a postdoctoral scholar in CFG.

The specific objective of the topology optimizer as used here is to be able to programmatically assign materials to the voxels of a panel such that its tilt angle is finely controlled based on distance from a magnet. A physical application would be, for example, to create a set of small reflectors that tilt to focus light to different focal points, assigned by the user, based on distance from the magnet.

Full details about the program are beyond the scope of this work, but the workflow is outlined here. Geometries and measurements from the experiment are used as inputs for the model. The model is able to assign values to previously unknown parameters, such as the shear modulus, based on a best fit to the data. Next, the program requires user input for desired specifications of future panels. Namely, the user should input two magnet distances and desired angle outputs. The program should then assign an optimized material layout.

The relevant results section, Section 6.3.2, briefly discusses preliminary achievements accomplished with the simulator and optimizer.

6 Results & Discussion

Magnetic field and actuator measurements are presented in this chapter in addition to a number of samples of 3D-printed multi-material, magnetically-actuated objects.

6.1 Magnetic Field

In Figure 6.1 the measured field intensity of the N52 magnet is plotted next to the analytic curve, with the input magnet polarization based on the measured value. The agreement of the two indicates that there can be confidence in using the analytic model for future simulations.

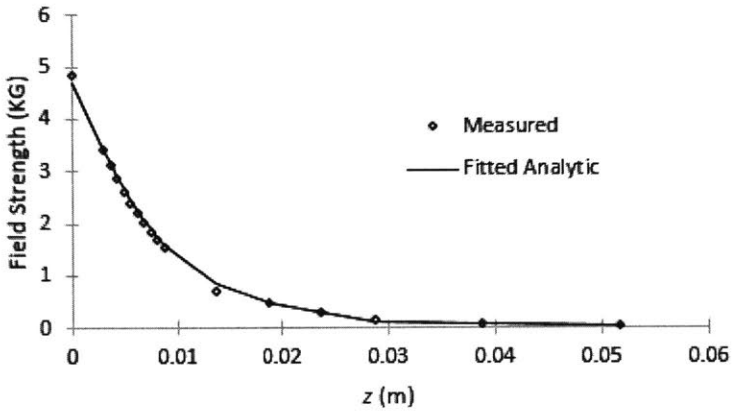

Figure 6.1: Measured field intensity at P = (0, 0, z) compared to the fitted analytic curve.

6.2 Fixed Cantilever

Performance of magnetic ink, measured primarily in terms of predictably of magnetic cantilever actuators, was tested and is compared here with the first-order theoretical model. To allow for easier comparison, results are grouped and presented based on a single varying parameter: FEO block thickness (t_{FEO}), cantilever length (l_{FEO}), or cantilever thickness (t_{FEO}). Note that if a graph ever shows the cantilever deflecting to a y_p = -0.014 m (the bottom of the plot), it means that the threshold was reached such that the cantilever was fully pulled in and collided with the magnet or, in the case of the theoretical model, was expected to do so.

6.2.1 *Varying FEO Block Thickness (Cantilevers 1, 2, and 3)*

Cantilevers 1, 2, and 3 all have the same cantilever length and thickness, but have a varying amount of FEO block thickness, t_{FEO}, with Cantilever 3 having the largest value. In Figure 6.2 the measured deflections (y_p) as a function of the magnet distance (d_{mag}) are plotted as data points alongside the iterative model (MATLAB) solutions which are connected by lines for clarity. Unfortunately only three measurements were collected for Cantilever 1 due to physical constrains of the testing set-up.

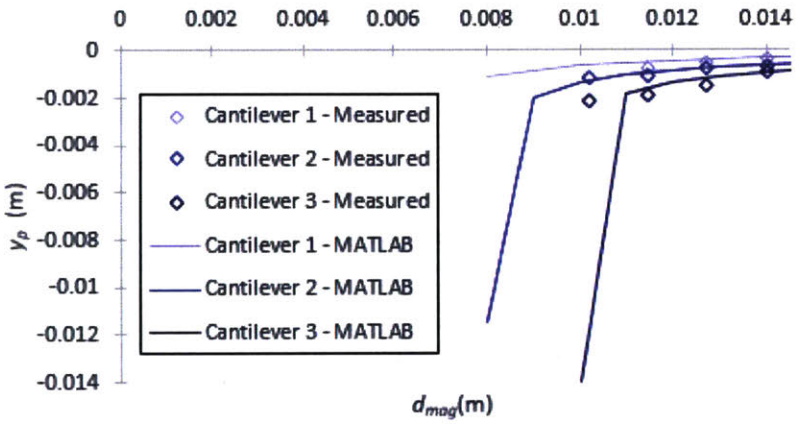

Figure 6.2: Measured versus expected (MATLAB) results are plotted. Increasing FEO block thickness corresponds with increasing darkness of the data, as shown in the legend.

The model shows relatively good agreement with the measured values. One discrepancy is that Cantilever 3 (dark blue) was estimated by the model to be fully pulled in by the magnet, which did not occur.

6.2.2 *Varying Cantilever Length (Cantilevers 1 & 4, 2 & 5, 3 & 6)*

Cantilevers 1 and 4, 2 and 5, and 3 and 6, are pairs of cantilevers that share all parameters except cantilever length, l_{RIG}. Cantilevers 4, 5, and 6 are the longer cantilevers in their respective pairs. Figure 6.3 shows results for all three pairs. In general, the model values for the shorter cantilevers (1, 2, and 3) are in better agreement with the measured values than those for the longer cantilevers. The model overestimates the deflection in all cases for the longer cantilevers, predicting collision sooner than it happened in reality.

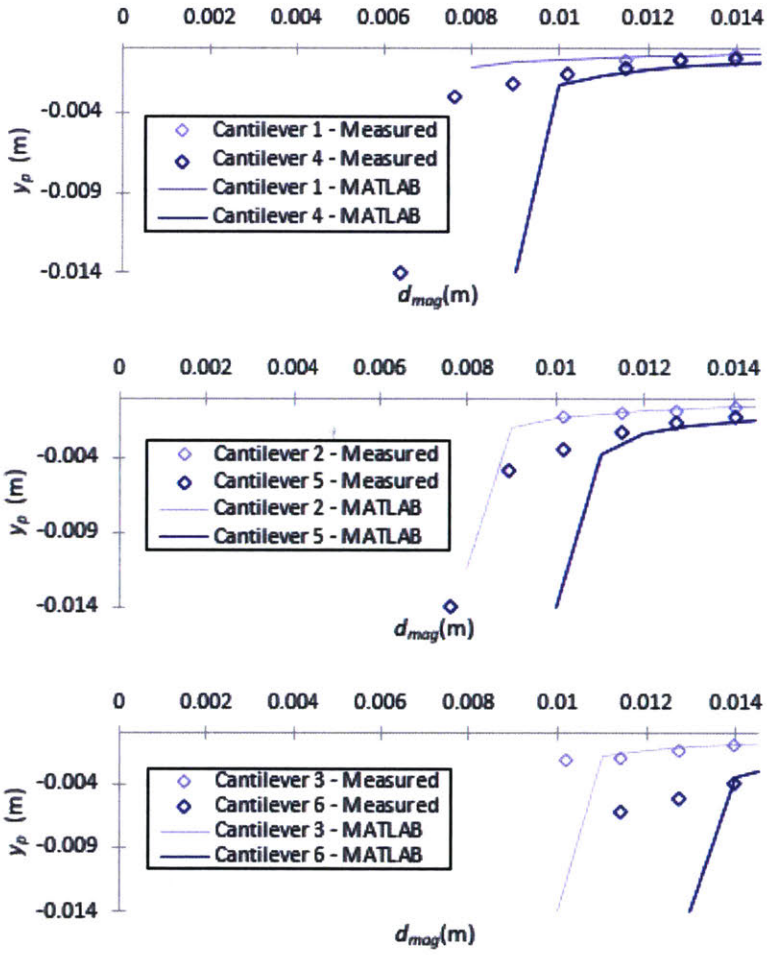

Figure 6.3: Measured versus expected (MATLAB) deflections are plotted for three different cantilever pairs, 1 and 4 (top), 2 and 5 (middle), 3 and 6 (bottom). The darker blue corresponds with the longer cantilever.

6.2.3 *Varying Cantilever Thickness (Cantilevers 6, 7, and 8)*

Cantilevers 6, 7, and 8 have the same FEO block size and cantilever length, but increase in thickness from Cantilever 6 to Cantilever 8. Results shown in Figure 6.4 indicate that the model predicts the varying differences between the starting deflections (d_{mag} = 0.014 mm) very well, but predicts final deflection rates and deflections less accurately. This is expected because the model is based on small deflection theory and the actual cantilevers deviate further from this assumption the more they are pulled in by the magnet.

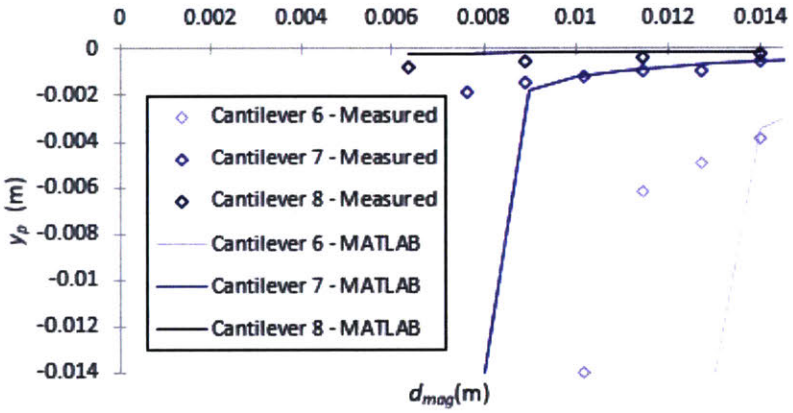

Figure 6.4: Measured versus expected (MATLAB) results are plotted. Increasing cantilever thickness corresponds with increasing darkness of the data, as shown in the legend.

6.2.4 *Discussion*

The measured and expected values show relatively good correspondence, especially given the number of approximations made for the model. The iterative model serves its purpose of providing first-order estimates of the expected behavior. Some of the plots show prominent deviation from the predictions, but there is no overall trend of underestimate or overestimation. It is likely that a portion of the error can be attributed to imperfections in the prints, which is particularly relevant for these thin, small structures. As can be noted from Figure 4.2, the print structures are not perfectly rectilinear. Sometimes, misfiring nozzles can cause other inconsistencies in the prints that are not as readily observed. This error could be minimized in the future by printing multiple copies of each cantilever and increasing the number of measurements taken for a given geometry. Furthermore, it would be interesting modify the MATLAB code and experimental set-up such that the exact "pull-

in" distance, the minimum distance of the magnet such that the cantilever is entirely pulled in, is predicted and measured. This would allow for a concise numerical evaluation of measured versus predicted results.

Naturally, this model can only be utilized for similar geometries, which limits its relevance to other applications. However, magnetically actuated cantilevers are powerful in their own right. For example, they can be used as resonators or microactuators.[52] Additionally, the same measurement set-up can now be used to characterize the material properties of the cantilever if it was a novel printed material.

6.3 Tilting Panel

Measured results from the tilting panels are presented and discussed alongside developments of the topology optimizer.

6.3.1 Angle Deflection Measurements

Figure 6.5 shows the results from the panel tilt measurements (see Section 4.2.2). The measurements for the three copies of each panel are averaged together. The measurements made at 0.5 m and 1 m are noted by their corresponding effective angles, Among each group of panels with the same number of layers of FEO, there is a generally downward trend on the plot for a given again. This is expected because as the panel number increases

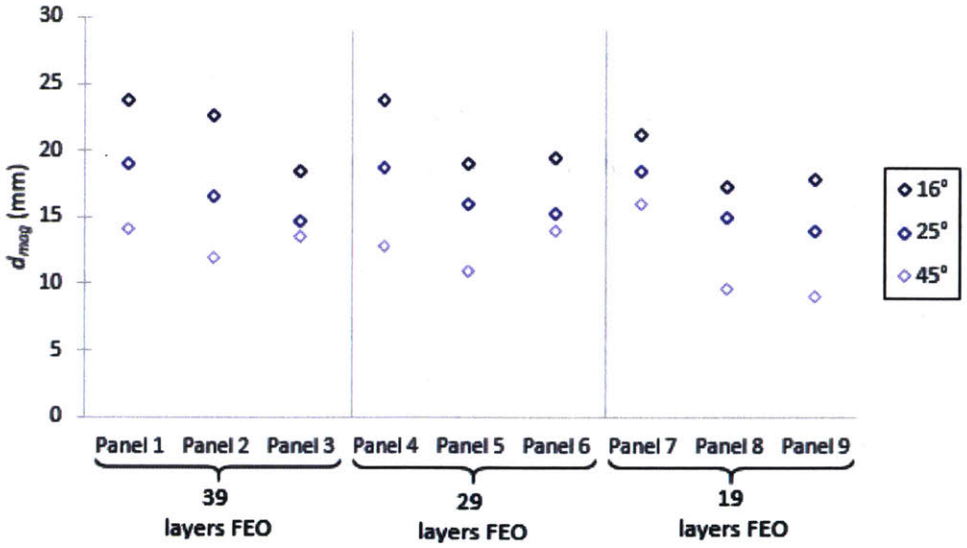

Figure 6.5: Plot of averaged (n=3) magnet distance from the print surface, d_{mag}, required to generate tilt angles of 16°, 25°, and 45°.

within a set, the thickness of the ELA joint increases in the geometry, requiring a strong field gradient, i.e. smaller distance from the magnet, d_{mag}. However, a number of the points deviate from the trend. The panel behavior is not as reliable as that of the cantilever. The deviation can likely be attributed to the sub-millimeter-sized ELA joint, which is very delicate and undergoes large deformation. For more repeatable results, the print geometries will likely need to be increased.

6.3.2 Simulator and Topology Optimizer

Figure 6.6a shows the optimizer's simulated representation of a panel tilted due to its position relative to the magnet. The parameters required to drive this model were fitted based on the tilting panel measurements. The objective of the optimizer is to output a material layout that will satisfy a user's request for two different panel tilt angles at two different distances from the magnet. By varying the distribution of FEO on one half of the panel (shown in blue in Figure 6.6a), some control of output angles is enabled. However, some requests are not physically possible given the geometric and material constraints. Figure 6.6b shows a range of achievable angle combinations for a given input of magnet distances based on geometry similar to that used in the panel tilting measurements. For a list of the model inputs for this example, see Appendix C: Optimizer Inputs. Each point in

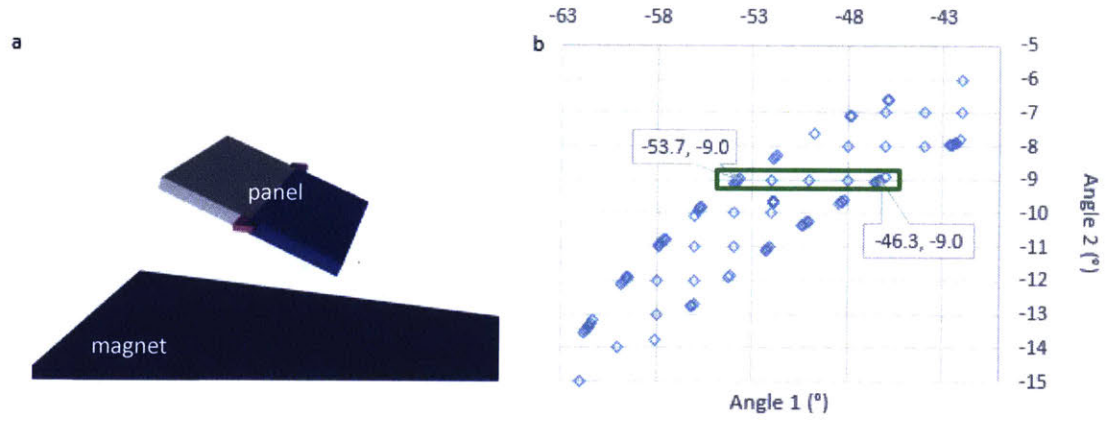

Figure 6.6: **a.** A labelled screenshot of the optimizer simulation showing the ELA joints (fuchsia) in torsion as the FEO portion of the panel (blue) is attracted to the magnet beneath it. **b.** Plotted data points represent angle combinations for which the optimizer is able to generate a material layout solution that fits within the provided geometry. The distance of the magnet that corresponds with Angle 1 and Angle 2, respectively, are 12.5 mm and 20 mm for this example.

the figure represents an angle combination for which the optimizer has generated a physically possible material arrangement. For example, the region highlighted by the green box and the two labelled data points show that two panels can have angles that differ by up to 7.4° when the magnet is nearby (d_{mag}= 12.5 mm) but are identical when the magnet is moved further away (d_{mag}= 20 mm).

6.4 Additional Structures

The following structures offer inspiration for future work and applications.

6.4.1 Functional Panel Arrays

The tilting tile was found to be very versatile. Small changes allowed the array to suggest new applications. Printed results are presented in Figure 6.7. Figure 6.7a shows how small-

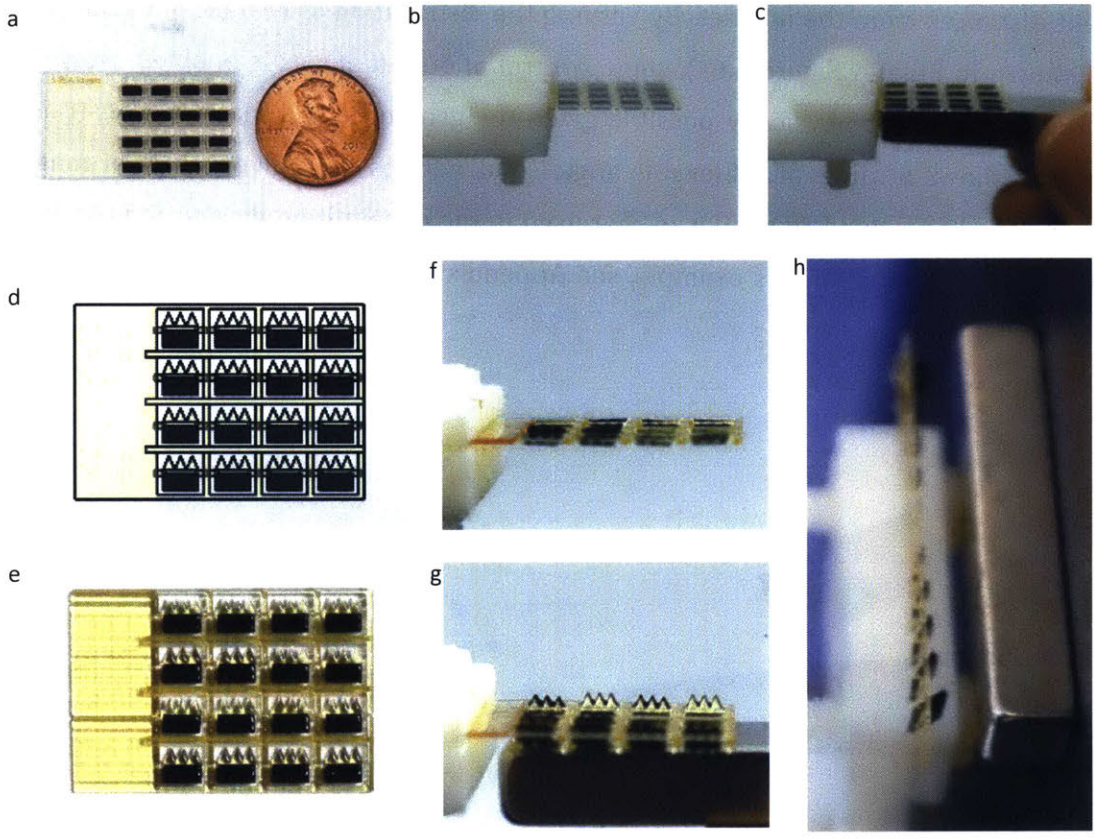

Figure 6.7: Tilting panel applications. **a** shows a 4 x 4 array of 3-mm panels, highlighting the high resolution achievable with this fabrication method. **b** and **c** are stills from a video showing a side view of the 4 x 4 array; the lifted panels act as flaps that affect the aerodynamics of the surface. **d** shows the target print result and **e** is the actual print. **f** and **g** are the same print in **e**, with and without the presence of a magnet, respectively. **h** shows an array of panels in which the concentration of FEO was varied to produce different tilt angles in the presence of a magnet.

scale the arrays can be. Figure 6.7b and 6.7c show how a small surface can become less aerodynamic when in the presence of a magnet. Figure 6.7d and Figure 6.7e allow for comparison of the target print (viewed from above) and the actual printed result. There are some grooves visible on the solid RIG portion of the printed results, evidence of inconsistent jetting. Figure 6.7f shows a side-view of the same structure and Figure 6.7g reveals the spikes of the panels sticking out in the presence of a magnet, reminiscent of a goosebumps-like response. Each spike was a wide of just 1 millimeter. Lastly, Figure 6.7h shows a linear array of panels that having varying concentrations of FEO such that the panels are actuated to different tilt angles in the presence of a magnet.

6.4.2 Double-Tilting Panel

Figure 6.8 shows that the printed double-tilting panel successfully achieves the goal of forming a concave "bowl" structure when held above a magnet. This 2 x 2 array demonstrates feasibility of creating panels with tilts that are fully tunable along two axes, which is compelling for optical applications. One notable issue, however, is that the functional area, that of the panels, is less than half of the total area, due to the additional frames and gaps required by the printing process. The ratio could be improved by increasing the panel size. However, to improve the ratio while maintaining small tiles would require better printer tolerances or a new design. The 2x2 array demonstrates feasibility of 2-axis control, but issues remain in terms of percent of functional area. A hexagonal tiling could offer improvement on this percentage.

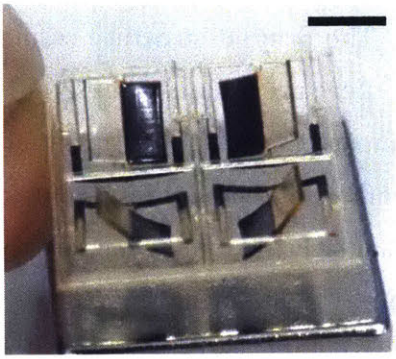

Figure 6.8: Double-tilting panel forms concave structure over magnet. Scale bar is 5 mm.

7 Conclusion & Future Work

In this chapter the thesis is summarized and suggestions are provided for future work.

7.1 Conclusion

This work is a stepping stone for future printing with magnetic ink in a multi-material inkjet 3D printer context. A reliably jetted magnetite ink has been developed and characterized. Multi-material actuators combining the magnetite ink with rigid and flexible inks were designed and printed. The deflection of the structures in the presence of a magnet was compared to structural and magnetic models, and the results showed that predictable actuators can be created. The results from the topology optimizer related to the tilt angle measurements provide a glimpse into the capabilities that can be enabled by programmatically assigning layouts in a multi-material, multi-field setting. It is exciting to imagine the applications that can be enabled by taking the printing of magnetic ink a step further, such as creating anisotropy in the print, which would open up the doors to torque-based actuations in a constant field. However, understanding the print characteristics of low loadings of magnetite nanoparticles and having a tool that enables fine control of printed actuators with this information is powerful in its own right. There is still room for exploring the bounds of printed technologies enabled by the magnetic ink formulation as it currently stands.

7.2 Future Work

This work makes a significant contribution in the form of a stable and reliably jettable magnetic ink for 3D printing. The printed structure results are suggestive of interesting future applications. However, there are a number of significant improvements that can be made to truly broaden the impact that magnetic materials can have in a multi-material context. In terms of print geometries, some minor adjustments could likely be made to increase the reliability of results. Prints could be smartly designed using the topology optimizer, and it would certainly be important to validate those programmed structures. However, the major strides to be gained are related specifically to the magnetic material.

The presented work relies on strong neodymium magnets for actuation because of the low volume percent concentration of the nanoparticles; this can be somewhat limited because

the control of the magnetic field is determined by the position of the magnet. A magnet does not have an on and off switch. Just doubling the nanoparticle content would help put the structures in a magnetization range that could be actuated by electromagnets; this would create a simpler way to control the field and hence the actuation. Increasing particle loading would also enhance the range of control that the proposed optimizer could then exploit.

The more limiting weakness of the developed magnetic ink is that it only allows actuation via magnetic body forces, which requires a field gradient. Extremely strong magnets are needed to create field gradients that are effective across distances significantly farther than the few centimeters spanned in this work. Strong fields are easier to create than strong gradients across long distances and large areas. Moreover, body forces offer far less control than torques. Magnetic torque is necessary to create forces that do more than simply pull the magnetic substance toward the field.

Anisotropic magnetization is needed to generate magnetic torques in prints. This could be achieved to some extent by exploring other nanoparticles for printing, as noted in Section 3.4.1. However, to fully utilize potential for magnetic torque actuation, the updated magnetic ink should likely also be paired with a new "magnetizer" module for MultiFab. The module could apply a magnetic field to a printed layer to control the magnetization direction during curing, similar to the techniques used in prior art[9,43,53]. A challenge exists for implementing this in that a number of the printer components are steel (attracted by magnetic fields) and that introducing a magnetic field nearby the printhead can cause agglomeration of particles in the printhead if not properly shielded.

Being able to print harder magnets or magnets with higher coercivity quickly opens the door to many more applications, such as imbedded tagging or information storage in printed objects, fully 3D-printed untethered miniature robots, or more advanced microfluidic prints.

Lastly, it is expected that continuing to pair this work with a topology optimizer will be important to fully exploit the power of 3D-printed magnetic material in a multi-material

context. It will become increasingly important to have programmatically assigned part layouts as geometries become more complex while still requiring fine control.

8 Appendix A: Ink Formulations

Tables indicate the full name of all ink components and their respective sources and gram content in a standard formulation.

ELA 7.2

Shorthand for ingredient	Full name/ description	Supplier	g
CN3105	Low viscosity acrylic oligomer	Sartomer, USA	48
SR504	Ethoxylated nonyl-phenol acrylate	Sartomer, USA	16
SR440	Isooctyl acrylate	Sartomer, USA	17
Genomer4215	Aliphatic urethane acrylate	Sartomer, USA	8
SR313B	Alkyl methacrylate	Rahn USA Corp.	10
Irgacure 819	Bis(2,4,6-trimethylbenzoyl)-phenylphosphineoxide	BASF, Germany	1
ITX	2-isopropylthioxanthone	Rahn USA Corp.	0.5
MEHQ	4-methoxyphenol	Sigma-Aldrich, USA	0.05

RIG 8.1

Shorthand for ingredient	Full name/ description	Supplier	g
Genomer2252/GP25	Bisphenol A epoxy diacrylate in 25% GPTA	Rahn USA Corp.	32
M300	Acrylic acid ester	Rahn USA Corp.	9
Genomer1117	Cyclic trimethylolpropane formal acrylate	Rahn USA Corp.	59
Irgacure 819	Bis(2,4,6-trimethylbenzoyl)-phenylphosphineoxide	BASF, Germany	1
MEHQ	4-methoxyphenol	Sigma-Aldrich, USA	0.1
ITX	2-isopropylthioxanthone	Rahn USA Corp.	0.5

EPX-100

Shorthand for ingredient	Full name/ description	Supplier	g
OC 2005	(3-4-Epoxycyclohexane) methyl 3'-4'-Epoxycyclohexyl-Carboxylat	IGM Resins USA Inc.	30
BPA diglycidyl ether	Bisphenol A diglycidyl ether	Sigma-Aldrich, USA	40
GE-13	Erisys GE13	Emerald Performance Materials, USA	30

9 Appendix B: MATLAB Code

The following code outputs expected deflection of the cantilever based on the distance of the magnet and input geometries and material properties. There is one original function within this code, *gradH*, which is an implementation of Equation 7. Are parameter are input in SI units.

```
function d_final = iterateddeflection (magdis)
t_RIG = .00011;
l_RIG = .01495; %point at which deflection is measured
t_FEO = .00142;
mu_0 = 4*pi*1e-7; %permeabilityofspace
E_RIG = 7e8; %Young's modulus
M_sat = 302000; %Magnetic saturation
W_FEO=.003;
l_FEO=.003;
percentvol_FEO=.019;

format long
%CALCULATIONS
%volume of iron oxide, assumes rectangular prism
V_m=feo_w*feo_l*feo_t;
canti_I = feo_w*canti_t^3/12;

%Iterate deflection until equilibrium
n=100;
count=1;
deflectioniterations = zeros(n,1);
[gradH_initial]= gradH(magdis, feo_t);
magforce = mu_0*V_m*percentvolfeo*M_sat*gradH_initial;
deflectioniterations(1) = magforce*canti_l^3/(3*rig_E * canti_I);
deflection=deflectioniterations(1);

for i=1:n
[gradH_iteration]= gradH(magdis+deflection, feo_t); %get new gradient and force
based on new position of cantilever
magforce = mu_0*V_m*percentvolfeo*M_sat*gradH_iteration;
deflectioniterations(i+1) = magforce*canti_l^3/(3*rig_E * canti_I);
deflection=deflectioniterations(i+1);
count=i+1;
    if deflectioniterations(i+1)-deflectioniterations(i)>-.000000001
        break
    end

    if -deflectioniterations(i+1)>magdis
        outputString = sprintf('Iteration %d causes colision',i)
        break
    end
end

d_final=deflectioniterations(count);

end
```

10 Appendix C: Optimizer Example Inputs

Inputs used to generate the plot in Figure 6.6b are listed below (see Section 4.2 for notation).

w_{ELA} = 0.5 mm

t_{ELA} = 0.175 mm

l_{free} = 0.5 mm

w_{gap} = 0.35 mm

M_S = 35 kA/m

$d_{mag}\ 1$ = 12.5 mm

$d_{mag}\ 2$ = 20 mm

11 Bibliography

1. Villar, G., Graham, A. D. & Bayley, H. A Tissue-Like Printed Material. 48–53 (2013).
2. Kang, B. J., Lee, C. K. & Oh, J. H. All-inkjet-printed electrical components and circuit fabrication on a plastic substrate. *Microelectron. Eng.* **97,** 251–254 (2012).
3. Guttag, M. & Boyce, M. C. Locally and Dynamically Controllable Surface Topography Through the Use of Particle-Enhanced Soft Composites. *Adv. Funct. Mater.* **25,** 3641–3647 (2015).
4. Gladman, A. S., Matsumoto, E. A., Nuzzo, R. G., Mahadevan, L. & Lewis, J. A. Biomimetic 4D printing. *Nat. Mater.* **15,** 413–8 (2016).
5. Ge, Q., Qi, H. J. & Dunn, M. L. Active materials by four-dimension printing. *Appl. Phys. Lett.* **103,** 131901 (2013).
6. Guiducci, L., Weaver, J. C., Bréchet, Y. J. M., Fratzl, P. & Dunlop, J. W. C. The Geometric Design and Fabrication of Actuating Cellular Structures. *Adv. Mater. Interfaces* **2,** (2015).
7. Erb, R. M., Libanori, R., Rothfuchs, N. & Studart, A. R. Composites Reinforced in Three Dimensions by Using Low Magnetic Fields. *Science (80-.).* **335,** 199–204 (2012).
8. Hu, J., Meng, H., Li, G. & Ibekwe, S. I. A review of stimuli-responsive polymers for smart textile applications. *Smart Mater. Struct.* **21,** 053001 (2012).
9. Kokkinis, D., Schaffner, M. & Studart, A. R. Multimaterial magnetically assisted 3D printing of composite materials. *Nat. Commun.* **6,** (2015).
10. Erb, R. M., Sander, J. S., Grisch, R. & Studart, A. R. Self-shaping composites with programmable bioinspired microstructures. *Nat. Commun.* **4,** (2013).
11. Burgert, I. & Fratzl, P. Actuation systems in plants as prototypes for bioinspired devices. *Philos. Trans. A. Math. Phys. Eng. Sci.* **367,** 1541–57 (2009).
12. Studart, A. R. Biologically inspired dynamic material systems. *Angew. Chem. Int. Ed. Engl.* **54,** 3400–16 (2015).
13. McEvoy, M. a. & Correll, N. Materials that couple sensing, actuation, computation, and communication. *Science (80-.).* **347,** 1261689–1261689 (2015).
14. Leong, T. G., Zarafshar, A. M. & Gracias, D. H. Three-dimensional fabrication at small size scales. *Small* **6,** 792–806 (2010).
15. Morgan, B. a. Developmental biology: a hair-raising tale. *Nature* **471,** 586–587 (2011).
16. Mäthger, L. M., Denton, E. J., Marshall, N. J. & Hanlon, R. T. Mechanisms and behavioural functions of structural coloration in cephalopods. *J. R. Soc. Interface* **6,** S149–S163 (2009).
17. Lang, A. W. *et al.* Movable shark scales act as a passive dynamic micro-roughness to control flow separation. *Bioinspir. Biomim.* **9,** (2014).
18. Wen, L., Weaver, J. C., Thornycroft, P. J. M. & Lauder, G. V. Hydrodynamic function of biomimetic shark skin: effect of denticle pattern and spacing. *Bioinspir. Biomim.* **10,**

(2015).

19. Zhu, Y., Antao, D. S., Xiao, R. & Wang, E. N. Real-time manipulation with magnetically tunable structures. *Adv. Mater.* **26,** 6442–6 (2014).

20. Erb, R. M., Martin, J. J., Soheilian, R., Pan, C. & Barber, J. R. Actuating Soft Matter with Magnetic Torque. *Adv. Funct. Mater.* (2016). doi:10.1002/adfm.201504699

21. Tseng, P. *et al.* Flexible and stretchable micromagnet arrays for tunable biointerfacing. *Adv. Mater.* **27,** 1083–9 (2015).

22. Kim, J. H. *et al.* Remote Manipulation of Droplets on a Flexible Magnetically Responsive Film. *Sci. Rep.* **5,** (2015).

23. Drotlef, D.-M., Blümler, P. & del Campo, A. Magnetically actuated patterns for bioinspired reversible adhesion (dry and wet). *Adv. Mater.* **26,** 775–9 (2014).

24. Judy, J. W., Muller, R. S. & Fellow, L. Magnetically Actuated , Addressable Microstructures. **6,** 249–256 (1997).

25. Tasoglu, S., Diller, E., Guven, S., Sitti, M. & Demirci, U. Untethered micro-robotic coding of three-dimensional material composition. *Nat. Commun.* **5,** 1–9 (2014).

26. Qiu, T. *et al.* Swimming by reciprocal motion at low Reynolds number. *Nat. Commun.* **5,** (2014).

27. Felton, S., Tolley, M., Demaine, E., Rus, D. & Wood, R. A method for building self-folding machines. 2–5

28. Makarov, D., Melzer, M., Karnaushenko, D. & Schmidt, O. G. Shapeable magnetoelectronics. *Appl. Phys. Rev.* **3,** (2016).

29. He, L., Wang, M., Ge, J. & Yin, Y. Magnetic assembly route to colloidal responsive photonic nanostructures. *Acc. Chem. Res.* **45,** 1431–40 (2012).

30. Timonen, J. V. I. *et al.* A Facile Template-Free Approach to Magnetodriven, Multifunctional Artificial Cilia. *ACS Appl. Mater. Interfaces* **2,** 2226–2230 (2010).

31. Misch, C. E. *Dental implant prosthetics.* (Mosby, 2005).

32. KUTERBACH, D. A., WALCOTT, B., REEDER, R. J. & FRANKEL, R. B. Iron-Containing Cells in the Honey Bee (Apis mellifera). *Science (80-.).* **218,** 695–697 (1982).

33. Schmidt, A. M. Electromagnetic Activation of Shape Memory Polymer Networks Containing Magnetic Nanoparticles. *Macromol. Rapid Commun.* **27,** 1168–1172 (2006).

34. Sitthi-amorn, P. *et al.* MultiFab : A Machine Vision Assisted Platform for Multi-material 3D Printing. *ACM Trans. Graph.* **34,** 129:1–129:11 (2015).

35. Derby, B. Inkjet Printing of Functional and Structural Materials: Fluid Property Requirements, Feature Stability, and Resolution. *Annu. Rev. Mater. Res.* **40,** 395–414 (2010).

36. Hilzinger, R. & Rodewald, W. *Magnetic Materials.* (2013).

37. Lu, A.-H., Salabas, E. L. & Schüth, F. Magnetic nanoparticles: synthesis, protection, functionalization, and application. *Angew. Chem. Int. Ed. Engl.* **46,** 1222–44 (2007).

38. Lin, E. Bio--inspired Design of Geometrically--Structured Suture Interfaces and Composites. (2015).

39. Mandel, K., Hutter, F., Gellermann, C. & Sextl, G. Synthesis and stabilisation of superparamagnetic iron oxide nanoparticle dispersions. *Colloids Surfaces A Physicochem. Eng. Asp.* **390,** 173–178 (2011).

40. Laurent, S. *et al.* Magnetic iron oxide nanoparticles: Synthesis, stabilization, vectorization, physicochemical characterizations and biological applications. *Chem. Rev.* **108,** 2064–2110 (2008).

41. Gupta, A. K. & Gupta, M. Synthesis and surface engineering of iron oxide nanoparticles for biomedical applications. *Biomaterials* **26,** 3995–4021 (2005).

42. Tiberto, P. *et al.* Magnetic properties of jet-printer inks containing dispersed magnetite nanoparticles. *Eur. Phys. J. B* **86,** 1–6 (2013).

43. Clay, G. *et al.* 3D Printing Magnetic Material with Arbitrary Anisotropy. *NIP Digit. Fabr. Conf.* **2015,** 307–310 (2015).

44. Voit, W., Zapka, W., Belova, L. & Rao, K. V. Application of inkjet technology for the deposition of magnetic nanoparticles to form micron-scale structures. *IEE Proc.-Sci. Meas. Technol* **150,** 252–256 (2003).

45. Inkyo, M., Tahara, T. & Imajyo, Y. New Nanoparticles Dispersing Beads Mill with Ultra Small Beads and its Application. *IOP Conf. Ser. Mater. Sci. Eng.* **18,** (2011).

46. Miranda, S. & Technologies, N. P. Using an agitator bead mill for nanoparticle dispersion and comminution. (2011).

47. Choi, H. J., Kim, C. A., M. Kwon, T. & Jhon, M. S. Viscosity of magnetic particle suspensions. *J. Magn. Magn. Mater.* **209,** 228–230 (2000).

48. Mooney, M. The viscosity of a concentrated suspension of spherical particles. *J. Colloid Sci.* **6,** 162–170 (1951).

49. McCaig, M. *Permanent Magnets in Theory and Practice*. (1977).

50. Yang, W., Tang, C. & Qin, F. Investigation of a cuboidal permanent magnet's force exerted on a robotic capsule. *Med. Devices Evid. Res.* **7,** 283–289 (2014).

51. Hibbeler, R. C. *Mechanics of Materials*. (2014).

52. Lagorce, L. K., Brand, O. & Allen, M. G. Magnetic microactuators based on polymer magnets. *J. Microelectromechanical Syst.* **8,** 2–9 (1999).

53. Kim, J. *et al.* Programming magnetic anisotropy in polymeric microactuators. *Nat. Mater.* **10,** 747–52 (2011).